

1 Spatial influence of fault-related stress perturbations in northern
2 Switzerland

3 Lalit Sai Aditya Velagala^{1,4}, Oliver Heidbach^{1,2}, Moritz Ziegler^{1,3}, Karsten Reiter⁴, Mojtaba Rajabi⁵, Andreas Henk⁴, Silvio
4 B. Giger⁶, Tobias Hergert⁷.

5 1 GFZ Helmholtz Centre for Geosciences, Telegrafenberg, 14473 Potsdam, Germany.

6 2 Institute for Applied Geosciences, Technische Universität Berlin, 10587 Berlin, Germany.

7 3 Professorship of Geothermal Technologies, Technical University Munich, 80333 Munich, Germany.

8 4 Institute of Applied Geosciences, Technische Universität Darmstadt, 64287 Darmstadt, Germany.

9 5 School of the Environment, The University of Queensland, QLD, 4072, Australia.

10 6 National Cooperative for the Disposal of Radioactive Waste, 5430 Wettingen, Switzerland.

11 7 Institute of Applied Geosciences, Karlsruhe Institute of Technology, 76131 Karlsruhe, Germany.

12 Correspondence

13 Lalit Sai Aditya Velagala: vlsar24@gfz.de; vlsadityareddy@gmail.com

14 Oliver Heidbach: heidbach@gfz.de

15 Abstract

16 The spatial influence of faults on the crustal stress field is a topic of ongoing debate. While faults are often known
17 to perturb the stress field at a meter scale, their lateral influence over a few hundred meters to several kilometers
18 remains poorly understood. To address this knowledge gap, we use a 3D geomechanical numerical model based
19 on 3D seismic data from northern Switzerland. The model is calibrated with 45 horizontal stress magnitude data
20 obtained from micro-hydraulic fracturing (MHF) and sleeve re-opening (SR) tests conducted in two boreholes in
21 the Zürich Nordost (ZNO) siting region, northern Switzerland. This model with seven faults implemented as
22 contact surfaces serves as the reference model in our study. The reference model is systematically compared to
23 three fault-agnostic models, which share identical rock properties, model dimensions, and calibration data with
24 the reference model, but differ in their element resolution and mechanical properties' assignment procedure.
25 Results show that at distances <1 km from faults, differences in maximum horizontal stress orientation between
26 models range from 3° – 6° , and horizontal stress magnitude differences are approximately 1–2 MPa. Beyond 1 km,
27 these differences reduce to $<1.5^{\circ}$ and <0.5 MPa, respectively. These differences are significantly smaller than the
28 calibration data uncertainties at ZNO, which average to ± 0.7 MPa and ± 3.5 MPa for the minimum horizontal and
29 maximum horizontal stress magnitude, respectively, and $\pm 11^{\circ}$ for the maximum horizontal stress orientation. An
30 important implication of our results is that, under the specific geological, mechanical, and stress conditions
31 observed at the ZNO siting region, explicit representation of faults may not be necessary in geomechanical
32 models predicting the stress state of rock volumes located a kilometer or more from active faults. This
33 simplification substantially reduced our model setup time from 2 months to 2 days, without compromising the
34 reliability of stress field predictions.

35 Short summary

36 We assess the fault impact on the stress field in northern Switzerland using 3D geomechanical models, calibrated
37 with stress data. We see that faults affect the stresses only locally, with negligible impact beyond 1 km,
38 suggesting that faults may not be necessary in reservoir-scale models predicting stresses of undisturbed rock
39 volumes, such as for a geological repository. Omitting them can substantially reduce model set-up time and
40 computational cost without compromising prediction reliability.

41 1. Introduction

42 Characterizing the crustal stress field is essential for understanding both global and local tectonic deformation
43 processes. On a large scale, it provides insights into plate tectonics (Richardson et al., 1979; Cloetingh and Wortel,
44 1985; Rajabi et al., 2017b) and earthquake mechanics (Sibson, 1992; Sibson et al., 2011; Brodsky et al., 2020),

45 while on a local scale, it plays a critical role in the safe planning of many subsurface applications, including oil
46 and gas exploration and storage (Berard et al., 2008; Zoback, 2009; Fischer and Henk, 2013), geothermal
47 exploration (Catalli et al., 2013; Schoenball et al., 2014; Azzola et al., 2019) and deep geological repositories for
48 nuclear waste (Long and Ewing, 2004; Gens et al., 2009; Jo et al., 2019). The present day stress state also
49 significantly impacts wellbore stability and trajectory optimization, reducing risks and improving drilling
50 operations (Kingsborough et al., 1991; Henk, 2005; Rajabi et al., 2016). Moreover, knowledge of the regional and
51 local stress field aids in assessing seismic hazards and understanding the potential generation or reactivation of
52 faults (Zakharova and Goldberg, 2014; Seithel et al., 2019; Vadacca et al., 2021).

53 The stress state at a point is described by the Cauchy stress tensor, a symmetric second-order tensor with six
54 independent components. This tensor can be transformed into a principal stress system, where only three
55 mutually perpendicular normal stresses, known as the principal stresses (S_1 = maximum principal stress; S_2 =
56 intermediate principal stress, and S_3 = minimum principal stress), remain, and the shear stresses are zero. In
57 reservoir geomechanics, where the target area is the upper crust, it is typically assumed that the principal
58 stresses are the vertical stress (S_v), the maximum horizontal stress ($S_{H\max}$), and the minimum horizontal stress
59 ($S_{H\min}$). Based on this, the reduced stress tensor is defined by the magnitudes of S_v , $S_{H\max}$, and $S_{H\min}$, and the
60 orientation of $S_{H\max}$ (Jaeger et al., 2007; Zoback, 2009).

61 The $S_{H\max}$ orientation is the most widely available, systematically documented, and freely accessible characteristic
62 of the reduced stress tensor, compiled in a publicly available database of the World Stress Map project (Heidbach
63 et al., 2018; Heidbach et al., 2025a). Analyzing the patterns of the $S_{H\max}$ orientation shows consistent trends over
64 hundreds of kilometers in intra-continental areas, primarily driven by first-order plate tectonic forces and
65 second-order buoyancy forces (Zoback et al., 1989; Zoback, 1992; Rajabi et al., 2017b; Heidbach et al., 2018). At
66 the same time, in some regions, significant rotations exceeding 30° are observed on spatial scales ranging from
67 a few tens to a few hundreds of kilometers. It is hypothesized that these variations in $S_{H\max}$ orientations, among
68 other reasons, arise from faults (Zoback et al., 1987; Yale, 2003; Heidbach et al., 2007; Tingay et al., 2009; Rajabi
69 et al., 2017b).

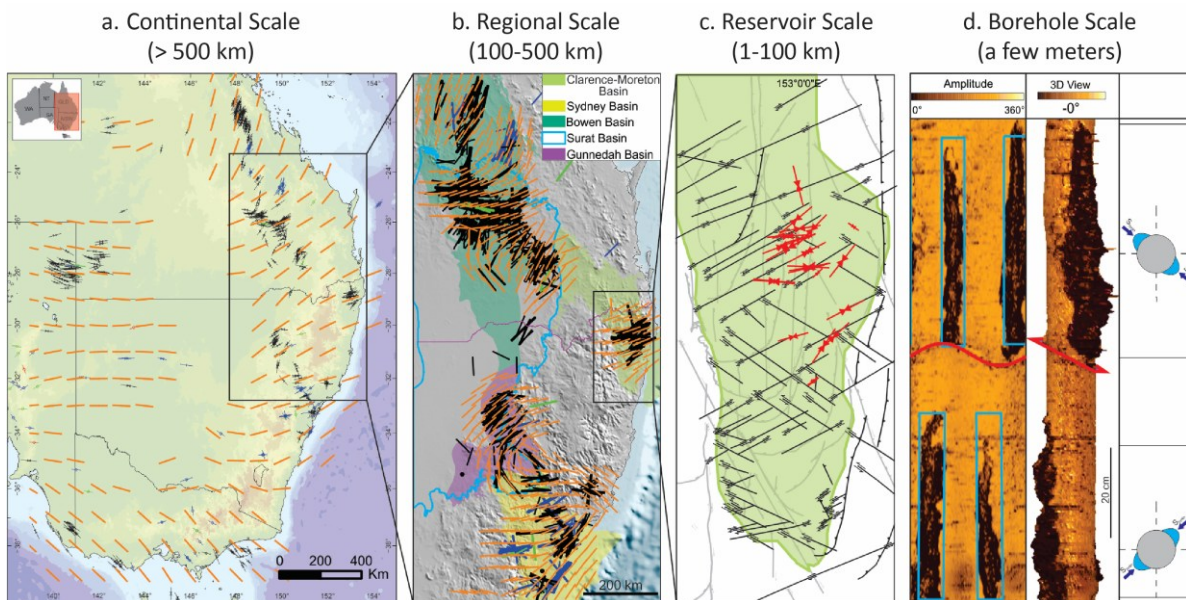
70 A common approach to understanding the fault impact on the stress field is to visually interpret laterally
71 scattered $S_{H\max}$ orientation data. This often leads to attributing the observed variability in $S_{H\max}$ orientation to the
72 faults present within their respective study areas (Yale et al., 1994; Bell, 1996b; Yale, 2003; Aleksandrowski et
73 al., 1992). While these studies are often convincing, they face two key issues: First, even in areas with relatively
74 high data coverage, such as northern Switzerland (Heidbach et al., 2025a; Heidbach et al., 2025b) and the
75 northern Bowen Basin (Rajabi et al., 2024; Heidbach et al., 2025a), the data density is fairly low, with, on average,
76 one data record per 138 km² lateral spatial distance, and one data record per 80 km² lateral spatial distance,
77 respectively. Second, individual $S_{H\max}$ orientations have an average standard deviation of ±15° (A-Quality) to ±25°
78 (C-Quality), as defined in the World Stress Map (Heidbach et al., 2025a). Together, these issues do not allow for
79 attributing with confidence small rotations in the $S_{H\max}$ orientations to the faults, especially at spatial scales of
80 0.1–10 km.

81 Notable studies from regions with a comprehensive $S_{H\max}$ orientation dataset show that large-scale faulting does
82 not necessarily result in abrupt rotations in the $S_{H\max}$ orientation over continental (>500 km) and regional scales
83 (100–500 km). For instance, in eastern Australia, the $S_{H\max}$ orientation rotates smoothly, by up to 50° over less
84 than 100 km despite varying dip and strikes of the major fault systems, from northern Bowen Basin to southern
85 Bowen and Surat basins (Brooke-Barnett et al., 2015; Tavener et al., 2017; Rajabi et al., 2024) (Fig. 1a-b).
86 However, in the adjacent Clarence-Moreton Basin, rotation of $S_{H\max}$ orientations is prominent and abrupt when
87 viewed in conjunction with the faults (Rajabi et al., 2015; Rajabi et al., 2017b; Rajabi et al., 2017c) (Fig. 1a-b).
88 Comparable conflicting trends have been reported in other studies as well (Bell and Gough, 1979; Gough and
89 Bell, 1982; Bell and Grasby, 2012), suggesting that the influence of fault systems on the rotation of $S_{H\max}$
90 orientation at continental and regional scales is not straightforward, and often not resolvable without ambiguity.

91 At the borehole scale, distinct variations in $S_{H\max}$ orientation have been observed vertically on a spatial scale of a
92 few meters. For instance, Fig. 1d shows an image log of a borehole from the Clarence-Moreton Basin, where the
93 $S_{H\max}$ orientation abruptly changes by 90° when the borehole intersects a fault. This is also observed in the San
94 Andreas Fault Observatory Drilling Borehole, where borehole breakouts (BO) and drilling-induced tensile
95 fractures (DITF) indicate a change in $S_{H\max}$ orientation from 25° ± 10° at 1000–1500 m to 70° ± 14° at 2050–2200

96 m (Chéry et al., 2004; Hickman and Zoback, 2004; Boness and Zoback, 2006; Zoback et al., 2011). Also, in the KTB
 97 drilling program, $S_{H\max}$ orientation along the borehole remained consistent with the regional tectonic-induced
 98 patterns except at a depth of 7200 m, where a major fault zone caused a localized reorientation by about 60°,
 99 confined to only a few meters above and below the fault (Brudy et al., 1993; Barton and Zoback, 1994; Brudy et
 100 al., 1997).

101 However, borehole-scale studies are generally conducted in vertical wells and do not capture the potential lateral
 102 variations in stress caused by faults. Therefore, it remains unclear whether these localized findings can directly
 103 be extrapolated to explain stress field variations at larger spatial scales away from the fault zone. This leads to a
 104 significant knowledge gap regarding fault's influence on stress field variations at the reservoir scale (Fig. 1c), a
 105 scale particularly important for many subsurface applications. The only viable approach for predicting the
 106 variations in the stress field at this scale is geomechanical numerical modelling. Over the past few decades, 2D
 107 and 3D geomechanical numerical models have been developed for this purpose (Henk, 2009, 2020; Treffeisen
 108 and Henk, 2020). These can broadly be grouped into three categories: 1) site-specific models without fault
 109 representation (Lecampion and Lei, 2010; Rajabi et al., 2017c; Ahlers et al., 2021), 2) site-specific models that
 110 include faults but are not explicitly focused on assessing influence of faults on the predicted stress (Reiter and
 111 Heidbach, 2014; Hergert et al., 2015; Bérard and Desroches, 2021) and 3) generic models that explicitly
 112 investigates the impact of faults (Homberg et al., 1997; Su and Stephansson, 1999; Reiter et al., 2024; Ziegler et
 113 al., 2024). While models without faults are understandably not suitable for evaluating fault-related stress
 114 perturbations, the latter two categories often have limited or no access to reliable *in situ* stress magnitude data.
 115 This hinders their ability to reliably represent fault-related stress variations in real-world scenarios.



116
 117 Figure 1: $S_{H\max}$ orientation stress map from eastern Australia at a) Continental scale; b) Regional scale; c) Reservoir scale, and
 118 d) Borehole scale. On continental and regional scales, visual observations suggest that faults may have differing influences,
 119 as seen in the uniform stress orientation (orange lines) across eastern Australia despite the presence of faults. However, on
 120 a borehole scale, faults can cause local perturbations, evident in the shift of borehole breakout orientations (blue box), which
 121 reflect stress variations across the fault (red line) (Image adopted from Rajabi et al. (2017c)).

122 In our study, we use 45 reliable and robust stress magnitudes data records, obtained from two deep boreholes,
 123 Trüllikon (TRU1-1) and Marthalen (MAR1-1), using microhydraulic fracturing (MHF) and dry sleeve re-opening
 124 (SR) test (Desroches et al., 2021a; Desroches et al., 2021b; Desroches et al., 2023) to calibrate 3D geomechanical
 125 numerical models of the Zürich Nordost (ZNO) siting region, northern Switzerland (Fig. 2). The data records were
 126 collected during a comprehensive 3D seismic and drilling campaign to support site selection for a deep geological
 127 repository (DGR) of radioactive waste (Nagra, 2024c, a). The stress magnitudes presented in this study are the
 128 total stresses, and any reference to the stress magnitudes must be taken as such. Four variants of the 3D
 129 geomechanical numerical model of the siting region, each with lateral dimensions of 14.7 km × 14.8 km, and a
 130 vertical depth of 2.5 km (below sea level; b.s.l), are used within this study. All models use identical mechanical

131 properties and the same representation of geomechanically relevant subsurface units. One of the models
132 includes seven contact surfaces with an assigned friction coefficient representing faults, and serves as the
133 reference model (REF model) (Nagra, 2024d, c), while the other three models are fault-agnostic, i.e., faults are
134 excluded from the model. By systematically comparing the predicted stress fields across all the models, we
135 illustrate the observed perturbations in the stress field with respect to the reference model and quantify the
136 spatial extent of the stress perturbations caused by faults.

137 2. 3D geomechanical numerical model with fault representation

138 2.1 Geological background and model geometry

139 The ZNO study region is located in the northern Alpine Foreland of northern Switzerland, approximately 30 km
140 NNE of Zurich (Fig. 2). It is close to the SW of Germany, where pre-Mesozoic basement rocks locally outcrop
141 (Nagra, 1984, 2002a). The geological evolution of this region was influenced by the development of a WSW–ENE
142 striking Permo-Carboniferous basin (Gorin et al., 1993; Mccann et al., 2006; Nagra, 2014), formed in response to
143 the Variscan orogeny and subsequent post-orogenic transtensional processes (Nagra, 1991; Marchant et al.,
144 2005).

145 During the Mesozoic, a sequence of sedimentary successions was deposited on top of the Variscan basement.
146 This depositional process was prominent, especially from the Early to Middle Jurassic due to a combination of
147 regional tectonic subsidence and sea level change (Coward and Dietrich, 1989; Nagra, 2024c). The sedimentary
148 rocks were originally deposited directly on the ocean floor as a result of the landmass corresponding to the
149 present day northern Switzerland being submerged in a broad and shallow epicontinental marine setting (Jordan,
150 2008; Reisdorf et al., 2011). The Opalinus Clay formation, deposited during the Jurassic Period of the Mesozoic
151 Era, is of particular importance as it has been selected as the host rock for Switzerland's DGR. Factors contributing
152 to the effectiveness of Opalinus Clay as a long-term geological barrier are its favorable mineralogy and associated
153 low permeability, and good sorption and self-sealing properties (Nagra, 2001, 2002b, 2008).

154 At the late Cretaceous and onset of the Cenozoic, the Alpine orogeny, formed by the collision of Adriatic and
155 Eurasian tectonic plates, led to a significant tectonic activity in the European northern Alpine Foreland (Illies,
156 1972; Schmid et al., 1996; Schmid et al., 1997; Cloetingh et al., 2006). This resulted in the formation of basement-
157 rooted, NNE-striking normal faults, forming the Upper Rhine Valley in combination with the uplift of the Black
158 Forest and Vosges Mountain Massifs. The formation of the flexural Molasse Basin during the Late Oligocene to
159 Early Miocene is a result of downbending of the European plate, in response to the orogenic loading of the Alps,
160 and caused a gentle dip from north to south in the Mesozoic strata (Sinclair and Allen, 1992; Kempf and Adrian,
161 2004; Sommaruga et al., 2012). In our study region, the Mesozoic strata gently dips SSE (Fig. 3). In the Late
162 Miocene, continued Alpine deformation propagated into the northern Foreland, resulting in the formation of the
163 Jura Mountains and their associated fold-and-thrust belt, primarily further to the west, and reactivating the pre-
164 existing basement structures (Diebold and Noack, 1997; Burkhard and Sommaruga, 1998; Laubscher, 2010).
165 These tectonic processes, along with the glacial-interglacial cycles during the Pleistocene (Fiebig and Preusser,
166 2008; Preusser et al., 2011), have established the present day geological and stratigraphic setting in the region.

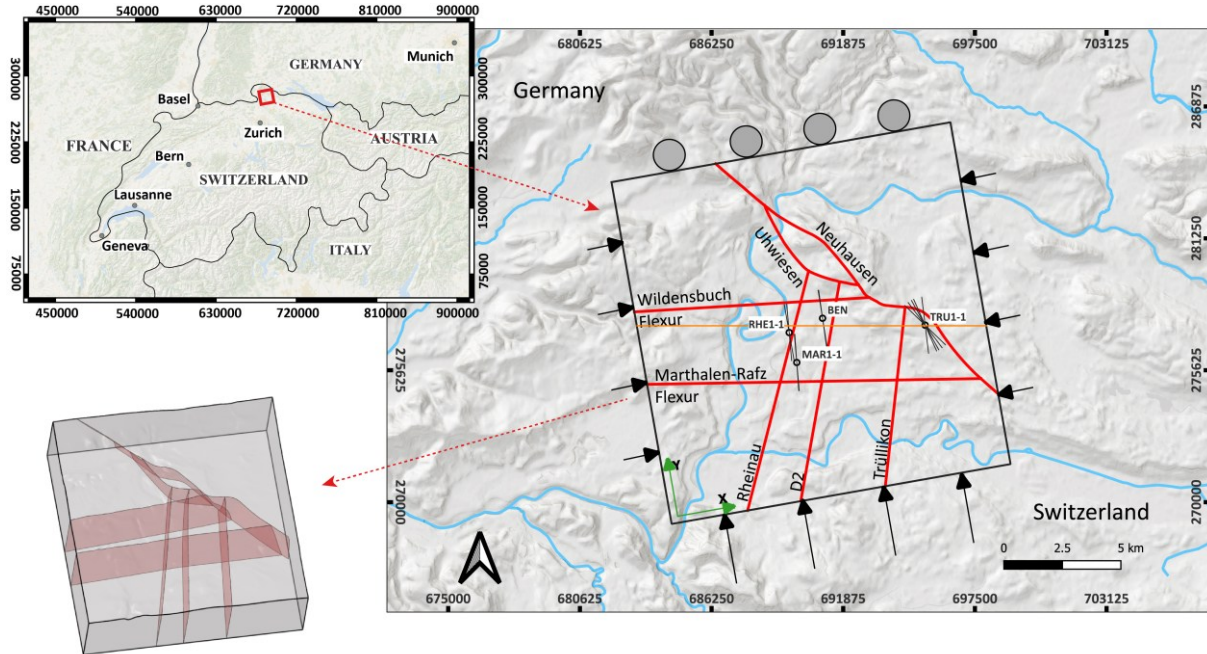
167 The reference model (REF model) is rectangular, spanning 14.7 km E-W × 14.8 km N-S laterally, and extending to
168 a depth of 2.5 km below sea level (b.s.l.). The upper boundary is defined by the local topography. In the siting
169 region, $S_{H\max}$ orientation is $170^\circ \pm 11^\circ$ according to the BO and DITF observations from the boreholes, in
170 agreement with the regional trend (Nagra, 2013; Heidbach et al., 2025b). To align the model geometry with the
171 $S_{H\max}$ orientation, the entire model domain is rotated by 10° counterclockwise from geographic north, such that
172 its sides are parallel and perpendicular to the mean $S_{H\max}$ orientation (Fig. 2).

173 The present day geomechanically relevant layers were constructed using SKUA-GOCAD v19 software. Successive
174 lithologies with comparable mechanical properties were combined (Table 1), eventually leading to 14
175 geomechanically different units in the REF model (Fig. 3). A total of seven faults and flexures, named Neuhausen,
176 Uhwiesen, Wildensbuch, Marthalen-Rafz Flexure, Rheinau, D2, and Trüllikon, were implemented in the model
177 (Fig. 2). These structures are modeled as contact surfaces, weakly interpreted from the regional 3D seismic
178 sections, and are highly simplified for ease of implementation in the model. Here, simplification means merging

179 much smaller segments interpreted on 3D seismics into larger, continuous fault planes to represent what is, in
180 reality, a volumetric fault zone structure (Nagra, 2024a) (Fig. 2, 3).

181

182



183
184 Figure 2: Geographical location and the model boundaries of the ZNO siting region. The red lines within the model extents
185 represent the surface trace of the faults and flexures, interpreted from the seismic sections of the siting region and
186 extrapolated to the surface. The location of the boreholes Trüllikon (TRU1-1), Benken (BEN), Marthalen (MAR1-1), and
187 Rheinau (RHE1-1) is shown, along with the $S_{H\max}$ orientation data records from each borehole (black lines with the centre at
188 the boreholes). The light brown line is the surface trace of a W-E cross-section, along which all the results in our study are
189 plotted. The black arrows on the sides of the model are the displacement boundary conditions. The grey circles in the north
190 of the model indicate that the displacements are constrained perpendicular to this boundary. The coordinate reference
191 system used is CH1903. The insert at the bottom left is the 3D view of the faults (light-red) within the model geometry (grey
192 box).

193 Both Neuhausen and Uhwiesen faults dip at 60° toward the northeast, while the others are vertical. Neuhausen
194 is the only fault that has a stratigraphic offset, with a vertical displacement of approximately 50 m at the base of
195 the Mesozoic units that decreases towards the surface (Nagra, 2002a, 2008, 2024d). The Marthalen-Rafz Flexur
196 and Wildensbuch Flexur are monoclines that dominate the overlying Mesozoic strata in the siting region through
197 a step-like bending rather than a discrete break in an otherwise dipping strata (Madritsch et al., 2024; Nagra,
198 2024c). Other than the Neuhausen fault, the remaining faults and flexures show no clear displacement but are
199 included in the model as they represent the first-order geological structures of the ZNO siting region.

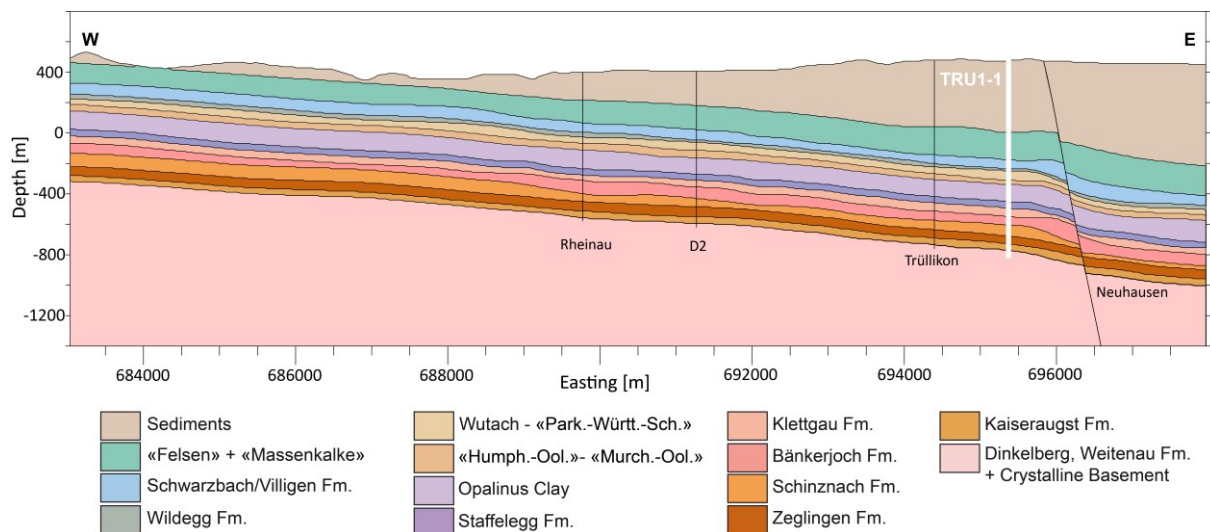


Figure 3: W-E cross-section of the geomechanical units passing through the Trüllikon borehole (bold white line, TRU1-1) and a constant northing = 277548 m within the REF model domain. The depth is referenced to the sea level. Vertical exaggeration by a factor of 2.5 is applied to enhance the visibility of thin layers, such as the Wildegg Formation. The respective mechanical properties are shown in Table 1. Only depths down to -1400 m (b.s.l) are shown for clarity, although the REF model extends to -2500 m (b.s.l). The coordinate reference system used is CH1903.

2.2 Reference model (REF model) setup

2.2.1 Model assumptions

The primary objective of the REF model is to reliably predict the present day stress state within the ZNO siting region. To achieve this, two key simplifying assumptions are made. First, transient effects such as time-dependent tectonic deformation or human-induced changes are neglected while considering only the stress contributions from the gravitational and tectonic forces. Since the model focuses on static stress field prediction, the rock volume is assumed not to undergo any transient deformation. Second, linear isotropic elasticity is assumed in the geomechanical units within the rock volume. This assumption simplifies the material parameters needed to explain the behavior of the rock under stress to just the Young's modulus which characterizes the elastic stiffness of the rock (E), Poisson's ratio which describes the lateral strain response (ν), and density (ρ) of each geomechanical unit. Throughout this work, we will refer to Young's modulus as stiffness and the contrast in Young's modulus as stiffness contrast. The equilibrium condition between the gravitational and the tectonic forces is governed by a second-order partial differential equation (PDE), with displacement as the field variable (Jaeger et al., 2007). Since this PDE cannot be solved analytically, a numerical solution is needed. Therefore, we use the Finite Element Method (FEM). FEM allows the use of unstructured meshes to represent the model volume, which is particularly useful when modeling complex geological features and variations in material properties (Mao, 2005; Henk, 2009).

Although several studies have shown that the stress state can be dominated by inelastic deformations once the elastic limits of the geomechanical units are exceeded (Smart et al., 2012; Pijnenburg et al., 2019; Yan et al., 2025), linear elasticity remains an appropriate first-order approximation for predicting the present day stress state in the ZNO siting region. This assumption is supported by several geological factors (Nagra, 2024d, c). The tectonic strain rates in northern Switzerland are extremely low, in the order of 1-3 m/Myr/km, and the region is tectonically stable, with no significant deformation observed since the Miocene. More importantly, the observed differential stresses (S_1-S_3) within the geomechanical units range between 0.5–13 MPa, which are significantly lower than their measured uniaxial compressive strength limits of 33–180 MPa. Because the differential stresses in the geomechanical units are far below their peak strength, plastic deformation is not expected under the current stress state.

2.2.2 Model discretization

235 The model setup follows a standard series of steps, previously used in other regional geomechanical studies
 236 (Buchmann and Connolly, 2007; Reiter and Heidbach, 2014; Hergert et al., 2015; Ziegler et al., 2016; Rajabi et al.,
 237 2017a). The model volume is discretized into 3D elements, collectively referred to as a mesh. The 3D element
 238 resolution plays a significant role in capturing predicted stress variations, where smaller elements capture a
 239 higher spatial resolution but at increased computational cost (Ahlers et al., 2021; Ahlers et al., 2022). To ensure
 240 a reasonably accurate representation of each geomechanical unit, a minimum of three finite elements is used in
 241 the vertical direction. Accordingly, the top 13 geomechanical units, which are relatively thin (Fig. 3), are
 242 discretized with smaller element sizes vertically, whereas the deeper and thicker Basement unit is represented
 243 with larger element sizes in the vertical direction. A total of 1,923,139 tetrahedral and hexahedral finite elements
 244 are used, providing a high-resolution representation of the geomechanical units, with model resolutions varying
 245 from 100-150 m laterally and 5-20 m vertically. We use first-order elements in this study, and the discretization
 246 is done using Altair HyperMesh 2021 software package.

247 2.2.3 Mechanical rock properties and fault properties.

248 Geological units with similar mechanical properties are grouped into the same geomechanical unit for simplicity.
 249 Each element in the mesh is assigned mechanical properties based on the corresponding geomechanical unit.
 250 The mechanical properties E [GPa], v [-], and ρ [kg/m³] used in the models are derived from petrophysical logs
 251 and from uniaxial and triaxial compression tests performed on the core samples obtained from the TRU1-1 and
 252 MAR1-1 boreholes (Nagra, 2024c, b). From the distribution of values for each geomechanical unit, the median
 253 values (P50) are used for the model, summarized in Table 1. Geological faults are implemented as contact
 254 surfaces that can slip under mechanical loading as a structural response to stress conditions, depending on their
 255 frictional properties. In the REF model, contact surfaces are assigned a friction coefficient of 1 and a zero
 256 cohesion, values chosen to best represent the fault properties in the region (Nagra, 2024c).

257 Table 1: Different geological formations with respective mechanical properties. The abbreviations are used solely to indicate
 258 the respective formations in the figures of this paper. Throughout the rest of this paper, the respective units can also be
 259 matched with the corresponding colors shown in Fig. 3 and with the abbreviations given here. Detailed information on the
 260 lithology is given in (Nagra, 2024c, b).

System	Group	Formation	Lithology	Abbreviation	ρ [kg/m ³]	v [-]	E [GPa]
Quaternary, Paleogene, and Neogene		Cenozoic Sediments	Sandstone (calc.)	CeSe	2350	0.30	15
Jurassic	Malm	«Felsenkalke» + «Massenkalk»	Limestone	MaFeMa	2685	0.18	31
		Schwarzbach-Villigen Fm.	Limestone (argill.)	MaScVi	2685	0.20	40
		Wildegg Fm.	Limestone	MaWi	2610	0.26	18
	Dogger	Wutach Fm.	Calc. marl	DoWuVaPa	2530	0.32	13
		Variansmergel Fm.	Silty marl				
		«Parkinsoni-Wütembergica-Sch. »	Silty marl				
		«Humphriesoolith Fm. »	Silty marl	DoHuWeMu	2540	0.28	14
		Wedelsandstein Fm.	Silty marl				
		«Murchisonae-Oolith Fm.»	Silty marl				
		Opalinus Clay Fm.	Silty claystone	DoOp	2520	0.37	11
	Lias	Staffelegg Fm.	Argill. marl	LiSt	2540	0.26	18
Triassic	Keuper	Klettgau Fm.	Dol. Marl	KeKl	2570	0.23	17
		Bänkerjoch Fm.	Anhydrite	KeBä	2700	0.22	23
	Muschelkalk	Schinznach Fm.	Dolostone, Limestone	MuSc	2710	0.24	32
		Zeglingen Fm.	Anhydrite	MuZe	2840	0.19	36

		Kaiseraugst Fm.	Argill. Marl	MuKa	2620	0.30	23
	Bundsandstein	Dinkelberg Fm.	Sandstone				
Permian	Rotliegend	Weitenau Fm.	Argill. Sandstone	DiWeCr	2540	0.27	34
Crystalline Basement		Crystalline basement.	Crystalline basement				

261 2.2.4 Model calibration

262 The present day stress state is computed by applying the gravitational forces and lateral displacement boundary
263 conditions to simulate the tectonic loading from the geological history. These boundary conditions are chosen
264 so that the modeled stresses best fit the measured horizontal stress magnitude data, a process known as model
265 calibration (Reiter and Heidbach, 2014; Ziegler and Heidbach, 2020).

266 In total, we have 30 $S_{h\min}$ and 15 $S_{h\max}$ magnitudes (Fig. 5). The $S_{h\min}$ magnitude ranges (Fig. 5: red bars) are derived
267 from the (MHF) tests and dry sleeve reopening (SR) tests (Desroches et al., 2021a; Desroches et al., 2021b;
268 Desroches et al., 2023; Nagra, 2024d) provide the basis to bracket the ranges for the $S_{h\max}$ magnitudes (Fig. 5:
269 blue bars). However, the mean of these ranges was used for the model calibration.

270 The model calibration is done using the PyFast Calibration tool (Ziegler and Heidbach, 2021), which uses a linear
271 regression-based algorithm to compute the best-fit lateral displacement boundary conditions by minimizing the
272 differences between the modeled and measured horizontal stress magnitudes. The resulting best fit for the
273 boundary conditions of the model volume was found to be a total shortening of 0.82 m applied in the east-west
274 direction, and 4.2 m in the north-south direction. Displacements parallel to the boundaries are permitted on all
275 lateral faces of the model. At the base, vertical displacement is constrained to zero, while horizontal
276 displacement is permitted; the model top remains fully unconstrained. The numerical solution is computed using
277 the Simulia Abaqus v2021 finite element solver. The results are analyzed using Tecplot 360 EX 2023 R2 along with
278 the Geostress v2.0 add-on library (Stromeyer et al., 2020).

279 3. Model set-up of 3D geomechanical numerical models without fault
280 representation

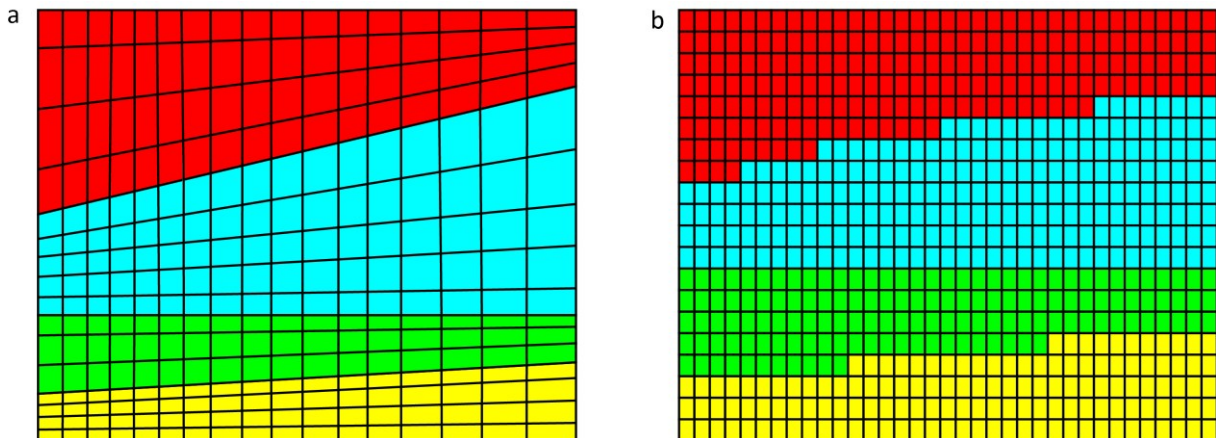
281 3.1 Model discretization strategies

282 Removing the fault implementation from the 3D models allows us to use different model discretization
283 strategies, which in turn significantly accelerates the model setup and stress prediction workflow. Using two
284 different discretization strategies, we developed three additional fault-agnostic 3D geomechanical numerical
285 models. The reference model and the three fault-agnostic models are then compared to quantify the spatial
286 influence of faults on the far-field stress state. In our study, the time required to build a model was reduced from
287 approximately two months for the reference model, the model that includes contact surfaces, to just two days
288 for the fault-agnostic models.

289 The standard procedure discretizes each geomechanical unit individually using the definition of its top and
290 bottom interface surfaces, and later connected by matching the nodes along the common interfaces. Each
291 element of the unit is assigned to the appropriate mechanical properties (Fig. 4a) directly from the stratigraphic
292 definition. While this approach results in a smooth unit boundary, it requires substantial manual effort and is
293 particularly time-consuming when working with models containing many geomechanical units.

294 In order to simplify the setup and discretization procedure of the fault-agnostic models, we use ApplePy
295 (Automatic Partitioning Preventing Lengthy Manual Element Assignment), a Python-based tool that automates
296 the discretization and element property assignment process (Ziegler et al., 2020). The entire model volume is
297 discretized in a single step as a largely homogeneous mesh, ignoring both lithological interfaces and fault
298 structures. ApplePy uses the depth values of the stratigraphic boundaries to decide which element belongs to
299 which lithological unit/geomechanical unit (Fig. 4b). Although this approach introduces step-like transitions at

300 unit boundaries which looks optically unrealistic, it significantly reduces the meshing time, especially for large or
 301 complex models, like the REF model without compromising the stress prediction capability of the final 3D
 302 geomechanical numerical models, as discussed in Sect. 4.



303
 304 Figure 4: A conceptual visual comparison of a) the standard procedure and b) the ApplePy procedure for discretization and
 305 mechanical property assignment to geomechanical units. The four colors represent distinct geomechanical units, each with
 306 unique lithologies and mechanical properties.

307 3.2 Model realizations and configurations

308 Building on the discretization strategies described in Sect. 3.1, three fault-agnostic 3D geomechanical numerical
 309 model realizations were developed. The three fault-agnostic 3D geomechanical numerical models follow the
 310 general model workflow of the REF model, i.e., the model parameterization and calibration are the same (Sect.
 311 2.2), along with the same model extents (Sect. 2.1). They are calibrated to the same dataset of 45 horizontal
 312 stress magnitude measurements used for calibrating the REF model. The only differences lie in the model
 313 discretization strategies (Sect. 3.1) and finite element resolution. Out of these three models, one is set up using
 314 the standard procedure, and two are set up using the ApplePy procedure. Table 2 presents the technical details
 315 on the number of elements and spatial resolution of each model used, along with the corresponding best-fit
 316 displacement boundary conditions obtained after applying FAST Calibration tool. The brief description of the
 317 three fault-agnostic models is:

- 318 • REF-NF model: Derived directly from the REF model with identical geometry, mesh and mechanical
 319 property assignments but with faults removed. Contact surfaces are eliminated, and opposing nodes
 320 are equivalenced, except for the Neuhausen Fault, where a 50 m lithological offset prevents node
 321 equivalencing. In this case, slip is prevented by assigning an artificially high friction coefficient of 50
- 322 • AP model: Maintains the same extents and mechanical properties as the REF and REF-NF models but
 323 uses ApplePy for property assignment to the elements. It does not incorporate faults and has
 324 approximately 50% more elements than the REF and REF-NF models.
- 325 • AP-H model: A higher resolution version of the AP model, with twice the number of elements. All the
 326 other features of the model are the same as the AP model.

327 Table 2: Summary of technical specifications for all model realizations used in this study. Reported vertical resolutions refer
 328 only to the Mesozoic units and are approximate for the ApplePy models due to depth-dependent variation. Minor differences
 329 in displacement boundary conditions reflect the presence of contact surfaces in the reference model, which allow elastic
 330 energy dissipation that is absent in the fault-agnostic models. The boundary conditions are compressional in nature.

Model realization	Discretization procedure	Number of elements	Vertical resolution of the mesozoic elements [m]	Lateral resolution [m]	Displacement boundary conditions	
					North-South shortening [m]	East-West shortening [m]
REF model	Standard procedure	1,923,139	5-20	100-150	4.1	0.82
REF-NF model		1,923,139	5-20	100-150	4.2	0.90

AP model	ApplePy procedure	2,826,240	~7 (non-basement units)	80–110	4.23	0.93
AP-H model		5,974,150	~4 (non-basement units)	60–80	4.25	0.90

331 4. Results

332 4.1 Stress magnitudes along borehole trajectories

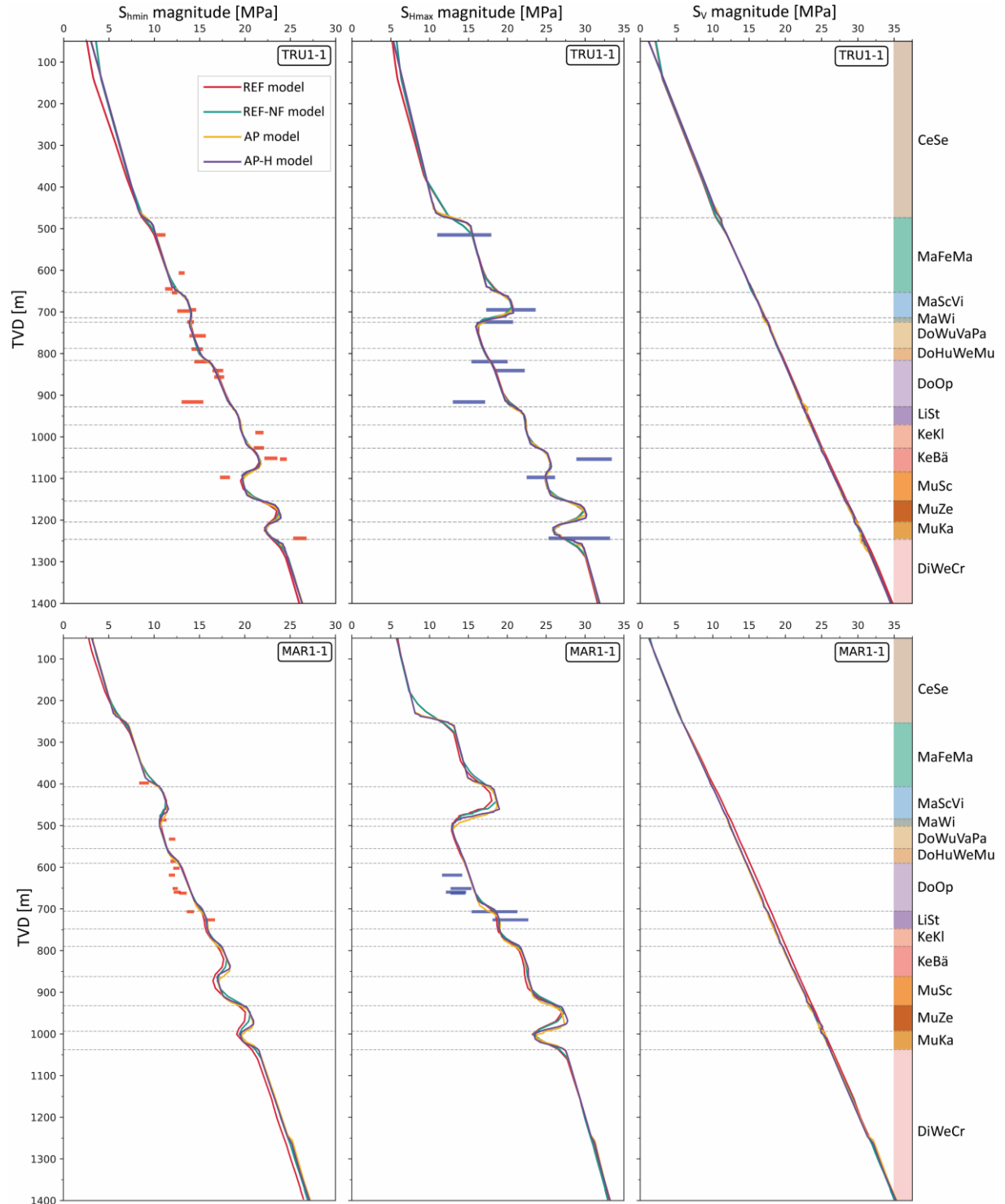
333 The resulting predicted stress magnitudes from all the model realizations are presented together with the
 334 measured $S_{h\min}$ (red bars) and estimated $S_{h\max}$ (blue bars) magnitude ranges along the TRU1-1 and MAR1-1
 335 borehole trajectories in Fig. 5. In general, the predicted horizontal stress magnitudes from the REF model align
 336 reasonably well with the measured stress ranges across different geomechanical units. However, some
 337 discrepancies are present, particularly in the Klettgau and Bänkerjoch formations, where the REF model
 338 underestimates $S_{h\min}$ magnitudes, and in the Schinznach formation, where $S_{h\min}$ magnitude is overestimated.
 339 These deviations arise because, for the model calibration, the REF model uses P50 (median) horizontal stress
 340 magnitude values despite the MHF tests resulting in ranges (red and blue bars in Fig. 5). Therefore, the stress
 341 predictions may vary from the assumed P50 value at a particular point in the subsurface. The vertical stress
 342 magnitude (S_v) is calculated from the weight of the overlying rock mass, considering the densities of the
 343 individual lithologies. From Fig. 5, it can be seen that S_v increases linearly with depth.

344 The predicted results from all the model realizations, regardless of fault implementation or exclusion, also align
 345 well with the measured horizontal stress magnitude ranges along both borehole trajectories across different
 346 geomechanical units, and are consistent with the REF model. Minor but negligible differences of <1 MPa in the
 347 $S_{h\max}$ magnitudes can be found at ~475 m (t.v.d) along the TRU1-1 borehole and at ~250 m (t.v.d) along the
 348 MAR1-1 borehole in the AP and AP-H models (Fig. 5). This is likely due to a high stiffness contrast between the
 349 Cenozoic sediments ($E = 15$ GPa) and Felsenkalke + Massenkalke ($E = 31$ GPa) units, the transition boundary of
 350 which is differently discretized due to ApplePy usage. A similar difference can be found at the Zeglingen Fm. ($E =$
 351 36 GPa), Kaiseraugst Fm. ($E = 23$ GPa) and the Dinkelberg, Weitenau Fm. and Crystalline basement ($E = 34$ GPa),
 352 which is also due to the widely varying stiffness contrasts.

353 Stiffer formations such as the Schwarzbach-Villigen Fm., Zeglingen Fm., and the basement have broader stress
 354 ranges in the measured data due to their statistically larger stiffness variability, while weaker formations like the
 355 Opalinus Clay exhibit narrower, more consistent stress distributions. Moreover, stiffer layers shield the weaker
 356 layers above and below, reducing stress variability in these formations. In short, Fig. 5 clearly indicates that the
 357 differences between the profiles from all the models are smaller than the measurement errors, represented by
 358 the length of the horizontal red and blue bars, and that the differences between the fault agnostic models and
 359 the REF model are insignificant. The variation of S_v magnitude with depth is consistent across all the model
 360 realizations, with differences <0.05 MPa observed between the models using ApplePy and the standard
 361 procedure.

362 The AP and AP-H models yield identical results. This indicates that increasing model resolution would not
 363 significantly improve stress predictions in our study and that the resolution of the AP model is already sufficient.
 364 This rules out resolution effects within the ApplePy models on the predicted stress magnitudes with respect to
 365 the REF model.

366



369 Figure 5: $S_{h\min}$ magnitude, $S_{h\max}$ magnitudes, and S_v magnitude of all the model realizations with depth (TVD) along the
 370 borehole trajectories of TRU1-1 (top row) and MAR1-1 (bottom row). The red and blue horizontal bars show the measured
 371 in-situ stress magnitude data of the $S_{h\min}$ and $S_{h\max}$, with lengths indicating their individual uncertainty (Nagra, 2024d, c). The
 372 geomechanical units are represented by their respective colors and abbreviations, consistent with Fig. 3 and Table 1.

376 4.2 Model results along a vertical cross-section and a horizontal layer

377 4.2.1 Horizontal differential stress ($S_{H\max}-S_{H\min}$)

378 Along the W-E cross-section through borehole TRU1-1, the horizontal differential stress ($S_{H\max}-S_{H\min}$) of the four
379 models displayed in Fig. 6a-d shows only small differences, except near the contact surfaces where noticeable
380 localized stress concentrations in the REF model occur. Similar result shows up when comparing the values of
381 $S_{H\max}-S_{H\min}$ along the mean Opalinus clay layer from the REF model (Fig. 6e) with those of REF-NF model (Fig. 6f).
382 To quantify the difference of the three fault-agnostic models w.r.t the REF model, Fig. 7a-c displays the difference
383 in the horizontal differential stress $\Delta(S_{H\max}-S_{H\min})$ between the models. The values of $\Delta(S_{H\max}-S_{H\min})$ exceed ± 2 MPa
384 only within 100 m of the fault. Beyond approximately 200 m from the faults, $\Delta(S_{H\max}-S_{H\min})$ across all models
385 becomes more similar to each other, and differences relative to the REF model typically remain below ± 0.4 MPa.
386 As the distance from the faults increases, the value of $\Delta(S_{H\max}-S_{H\min})$ differences rapidly decreases.

387 In addition to the spatial proximity to contact surfaces, the variation of $S_{H\max}-S_{H\min}$ depends on the stiffness of the
388 geomechanical units. In specific Mesozoic units characterized by lower stiffness, such as from the Wildegg Fm.
389 of the Malm Group to the Klettgau Fm. of the Keuper group, and the Kaiseraugst Fm. of the Muschelkalk group
390 (Table 1), the $S_{H\max}-S_{H\min}$ typically is <3.5 MPa. In contrast, units with high stiffness can exhibit $S_{H\max}-S_{H\min}$
391 exceeding 7 MPa, such as in the «Felsenkalke» + «Massenkalk» and the Schwarzbach-Villigen Fm. of the Malm
392 group, Schinznach and Zeglingen Fm. of the Muschelkalk group and the Dinkelberg Fm., Weitenau Fm. and
393 Crystalline basement (Fig. 6a-d, Table 1). This trend is expected, as lower stiffness materials accommodate
394 deformation more readily, resulting in lower differential stresses, whereas stiffer units resist deformation,
395 leading to higher differential stresses. The Opalinus Clay layer has a Young's modulus of 11 GPa, which is relatively
396 low compared to the other geomechanical units present in the siting region. The adjacent stiffer geomechanical
397 units act as stress-bearing members, effectively shielding the soft layer and further reducing the stress
398 magnitudes concentrated within it. The $S_{H\max}-S_{H\min}$ in the mean Opalinus Clay layer, as predicted by the models,
399 is <2 MPa irrespective of fault inclusion or exclusion from the model (Fig. 6e-f).

400 A particularly notable observation is that the differential stress near the Neuhausen fault remains relatively
401 comparable across all models when compared to the magnitude of differences in $S_{H\max}-S_{H\min}$ at other contact
402 surfaces. Despite the Neuhausen fault being either fully removed or mechanically disabled via a high friction
403 coefficient, the differential stress pattern across the 50-meter offset between the footwall and the hanging wall
404 is well replicated in the AP and the AP-H models in Fig. 6a-d. This is attributed to the abrupt contrast in mechanical
405 properties across the Neuhausen Fault (Fig. 3; Table 1), which effectively mimics the local stress response, even
406 in the absence of explicit fault representation.

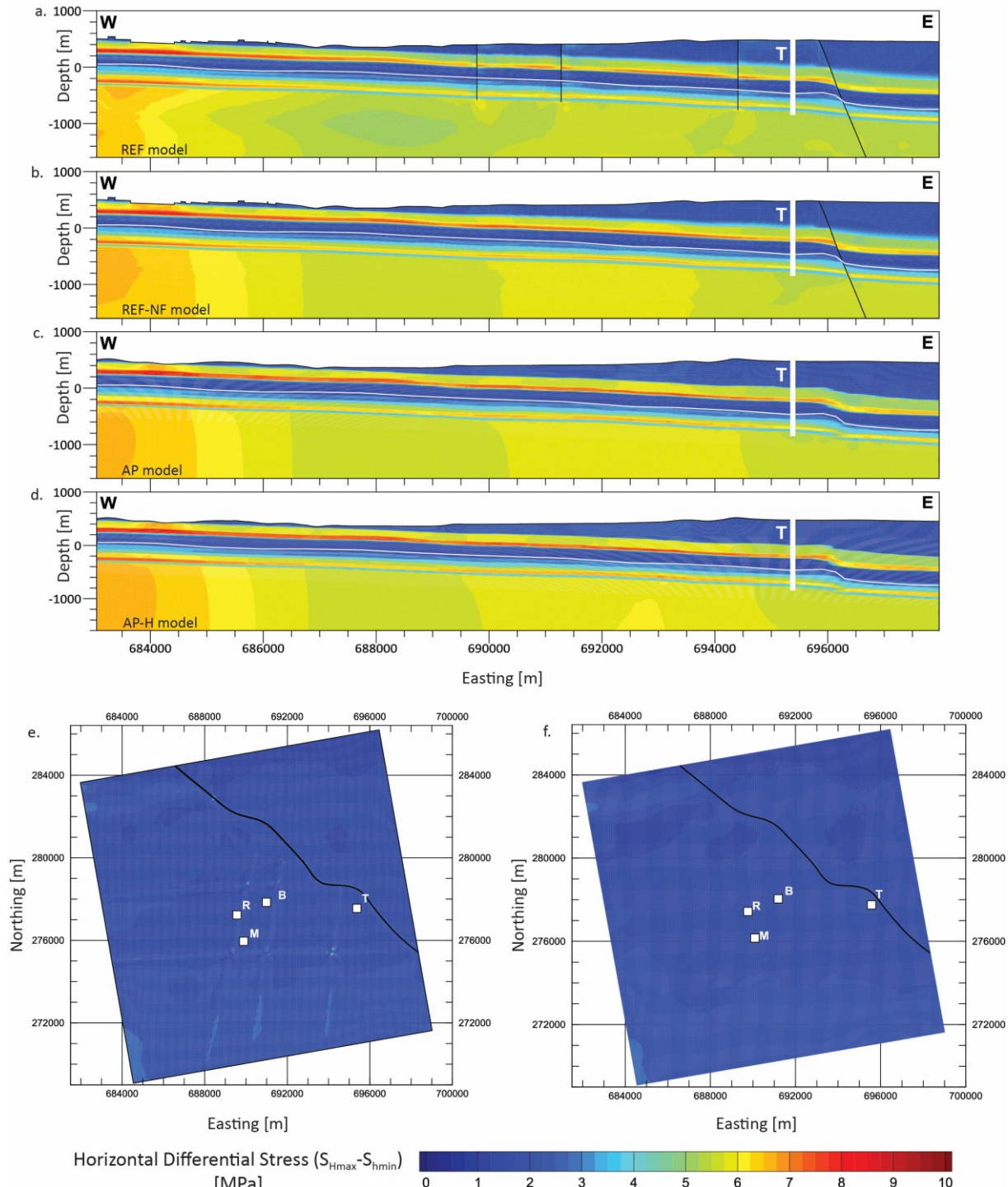
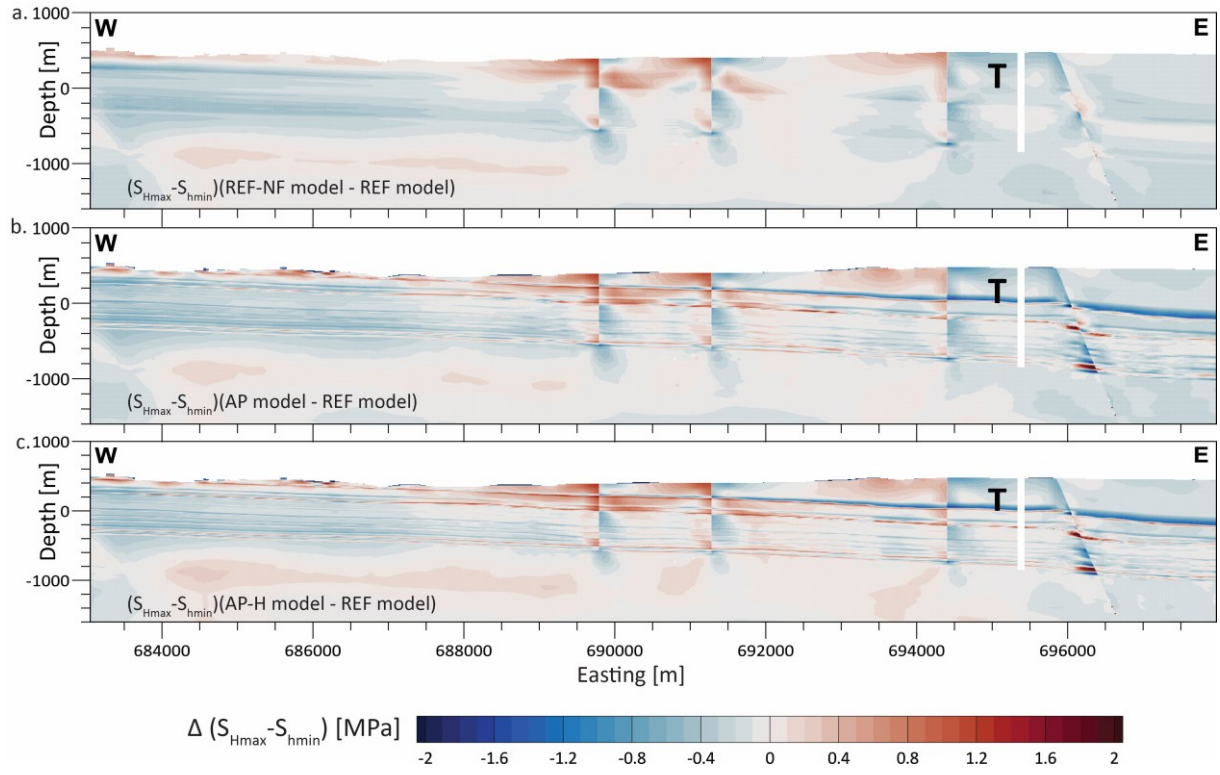


Figure 6: a-d) Modelled horizontal differential stress ($S_{Hmax} - S_{Hmin}$). a-d) W-E cross section (brown line in Fig. 2) through the TRU1-1 borehole (white vertical bar) with depths referenced to below sea level (b.s.l.). The location of faults is indicated by black lines. e-f) Mean Opaline Clay layer of the REF and REF-NF model, indicated by the white lines on the W-E cross sections. Capital letters indicate the location of the four boreholes TRU1-1 (T), BEN (B), MAR1-1 (M), and RHE1-1 (R).



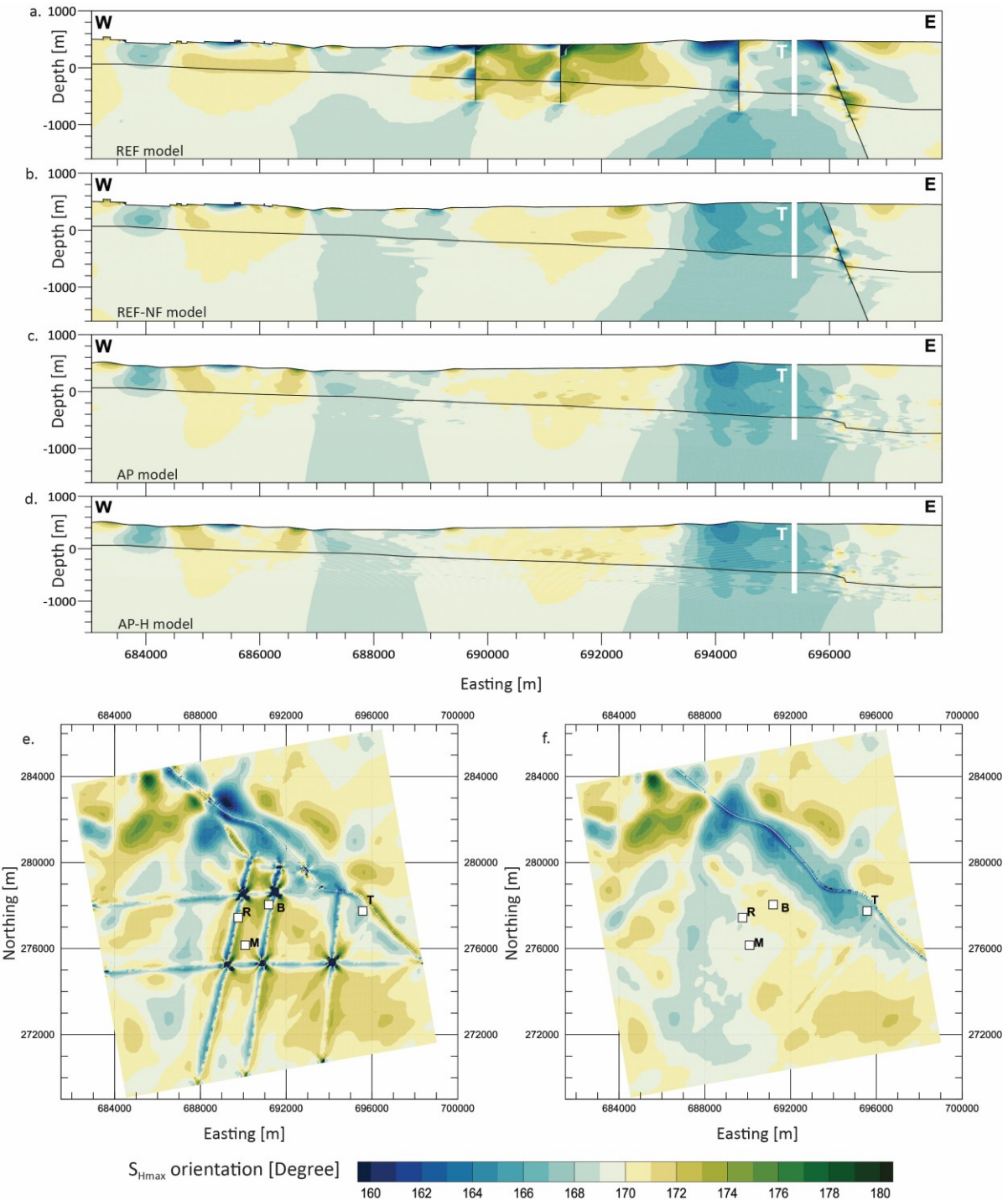
413

414 Figure 7: a-c) Difference of $S_{H\max}$ - $S_{h\min}$ between the models without faults and the REF model with active faults along the same
 415 cross-section as in Fig. 6. The cross-sections show the difference with respect to the REF model and are indicated at the
 416 bottom left of each slice. Although faults have not been directly indicated on the cross-sections, the location of the faults can
 417 be visually seen as sudden lateral changes in an otherwise continuous change in $\Delta(S_{H\max}-S_{h\min})$.

418 4.2.2 $S_{H\max}$ orientation

419 Along the same W-E cross-section as in Fig. 6a-d, the $S_{H\max}$ orientation of the four models is displayed in Fig. 8a-
 420 d, and the variability of the $S_{H\max}$ orientation w.r.t the REF model is displayed in Fig. 9a-c. Fig. 8e-f shows the
 421 variability of $S_{H\max}$ orientation along the mean Opalinus clay layer from the REF model and the REF-NF model
 422 respectively.

423 The largest $S_{H\max}$ orientation variability is reoriented more within a distance of 100–200 m around the contact
 424 surfaces, similar to the observations of $\Delta(S_{H\max}-S_{h\min})$. At this distance, differences greater than 6° w.r.t. the REF
 425 model are observed. These differences tend to reduce to less than $\pm 2^\circ$ at lateral distances greater than 500 m
 426 from the contact surfaces. Within the near-field zone, which is <300 m from the contact surfaces, stress
 427 concentrations are probably artifacts arising from the numerical resolution limit. This shift in $S_{H\max}$ orientation
 428 can also be observed in Fig. 8e-f along and near the contact surfaces. Even under a hypothetical assumption that
 429 the observed variations are entirely fault-induced, the current stress indicator techniques cannot resolve $S_{H\max}$
 430 variations within 10°. Therefore, these differences can be considered insignificant and non-resolvable. Finally,
 431 increasing model resolution does not change our results, as seen when comparing the AP and AP-H model results
 432 in Fig. 8 and Fig. 9.

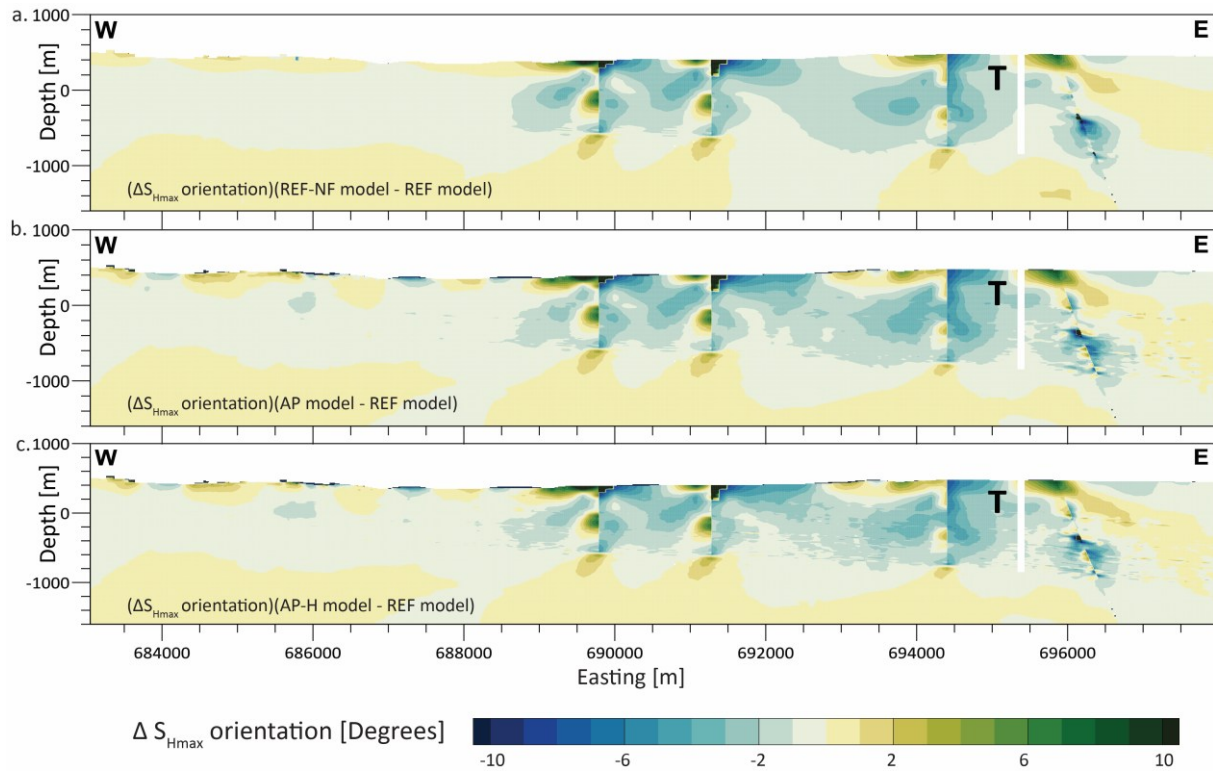


433

434 Figure 8: Absolute S_{\max} orientation. a-d) W-E cross-section through borehole TRU1-1 (T) indicated with the white vertical
 435 bar. e-f) Mean Opalinus Clay layer of the REF and REF-NF model, indicated by the black lines on the W-E cross sections. Capital
 436 letters indicate the location of the four boreholes TRU1-1 (T), BEN (B), MAR1-1 (M), and RHE1-1 (R).

437

438



441 Figure 9: a-c) Difference of S_{Hmax} orientation between the models without faults and the REF model with active faults along
 442 the same cross-section as in Fig. 7. The cross-sections show the difference with respect to the REF model and are indicated
 443 at the bottom left of each slice. Although faults have not been directly indicated on the cross-sections, the location of the
 444 faults can be visually seen as sudden lateral changes in an otherwise continuous change in ΔS_{Hmax} orientation.

445 4.3 Quantification of the lateral extent of fault-induced stress changes.

446 To better quantify the impact of faults on stress, we interpolated the results of the four models on a SW-NE
 447 oriented horizontal line at 300 m (b.s.l) crossing five of the seven faults (Fig. 10a-c). To improve readability, the
 448 results from the AP model were not plotted, as it is clear from Figs. 5, 7, and 9 that the AP and AP-H model results
 449 are almost identical.

450 The S_{Hmax} and S_{hmin} magnitudes of different model realizations largely overlap each other along the horizontal
 451 line. A difference of ~ 0.5 MPa is observed in S_{Hmax} magnitude (Fig. 10b), and ~ 1 MPa is observed in the S_{hmin}
 452 magnitudes (Fig. 10a) between the REF model and the fault-agnostic models, within ~ 500 m of the faults.
 453 However, these differences are less than the widths of the stress magnitude data, which in turn, represent the
 454 uncertainty of the measurements (Fig. 5). In general, the horizontal stress magnitudes from the REF model have
 455 an abrupt change in the vicinity of the faults, deviating from the continuous trend followed by other model
 456 realizations. The differences in the S_{Hmax} magnitudes reduce to < 0.2 MPa beyond a distance of about 500 m from
 457 the fault. The differences in the S_{hmin} magnitudes follow the same pattern as the S_{Hmax} magnitude, and also reduce
 458 beyond a distance of about 500 m away from the fault.

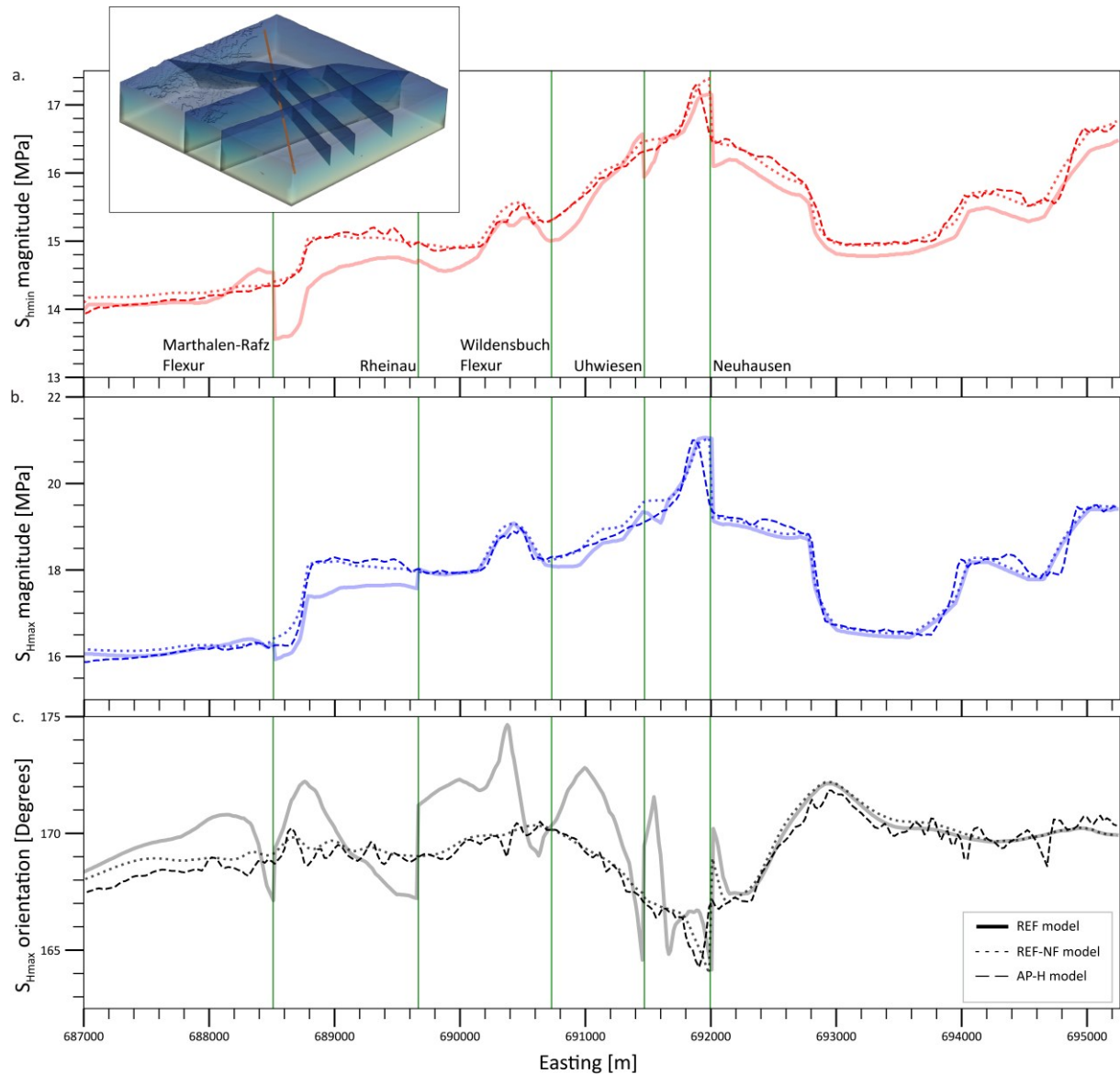
459 Similarly, the S_{Hmax} orientation of the REF model shows negligible deviations of $< 2^\circ$ in the undisturbed rock
 460 volume, away from the faults, and a deviation of 2° – 6° up to 1 km from the modeled faults (Fig. 10c). According
 461 to the quality ranking scheme of the S_{Hmax} orientation from the World Stress Map, the A-quality data, data of the
 462 highest quality, has a standard deviation of $\pm 15^\circ$ (Heidbach et al., 2025a). Even S_{Hmax} orientations derived from
 463 the DITF and BO in the MAR1-1 and TRU1-1 boreholes exhibit standard deviations of approximately $\pm 11^\circ$.
 464 Considering this, the orientation deviations seen in Fig. 10c are not resolvable and well below the uncertainties
 465 of the in situ indicators.

466 Near the Neuhausen fault, there is a localized abrupt change in the horizontal stress magnitudes within ~ 100 m
 467 on either side of the modeled fault for all the model realizations. An important observation is that this abrupt

468 change occurs not only in the REF model but also in the models without any faults. These stress changes are
 469 primarily controlled by the lateral stiffness contrasts due to the offset and not by the mere presence of the faults.

470 Overall, the differences are <0.2 MPa in stress magnitudes and <2° in $S_{H\max}$ orientations beyond 1 km from the
 471 fault, which is far less than the uncertainties of the horizontal stress magnitude data from the MHF and the SR
 472 tests, as well as the stress indicators for the $S_{H\max}$ orientation from the boreholes. Even in a conservative
 473 approach, it is clear that the effect of faults on the stress field is within about 1 km from the fault core. This
 474 conclusion aligns with the findings by Reiter et al. (2024), who, through generic model studies, found that
 475 significant stress changes due to faults only occur within a distance of a few hundred meters, partly up to 1 km
 476 next to the fault.

477



478

479 Figure 10: Magnitudes of $S_{H\min}$ and $S_{H\max}$, and the $S_{H\max}$ orientation along a SW-NE horizontal profile at 300 m (b.s.l.), shown
 480 in the 3D figure as a red line. Green vertical lines with the respective fault names denote the location where the profile crosses
 481 the modelled faults.

482

483 5. Discussion

484 5.1 Comparison with observed $S_{H\max}$ orientation data

485 The $S_{H\max}$ orientation is the most widely available characteristic of the reduced stress tensor. It is also the easiest
486 to analyze because it can be averaged and visualized with respect to the fault on stress maps (Fig. 1) (Yale et al.,
487 1993; Yale et al., 1994; Yale and Ryan, 1994; Yale, 2003; Rajabi et al., 2017c; Heidbach et al., 2018). The $S_{H\max}$
488 orientation can be determined from different stress indicators, such as from direct borehole-based indicators,
489 earthquake focal mechanisms, geological indicators, or passive seismic methods (Amadei and Stephansson,
490 1997; Zang and Stephansson, 2010; Heidbach et al., 2025a). Among these, direct borehole-based indicators such
491 as borehole breakouts (BOs), drilling-induced tensile fractures (DITFs), and hydraulic fracturing (HFs) are
492 commonly considered to be the most reliable (Bell, 1996a; Zang and Stephansson, 2010).

493 In the ZNO study region, 11 $S_{H\max}$ orientation data records are available from HFs, DITFs, and BOs. The mean $S_{H\max}$
494 orientation from these data is 170° with a standard deviation of $\pm 11^\circ$ (Nagra, 2024d, c; Heidbach et al., 2025b). The individual standard deviation of each data record is between $\pm 9^\circ$ and $\pm 19^\circ$, indicating that rotations $<\pm 11^\circ$
495 cannot be resolved. As the differences between the REF model and the three fault-agnostic models, as displayed
496 in Fig. 9, are smaller than $\pm 10^\circ$, the potential impact cannot be resolved with any stress indicator. Furthermore,
497 most of the rotations observed are located close to the fault. At a distance of 1000 m from a fault, the rotation
498 is $<\pm 2^\circ$ and thus clearly below the uncertainties of any measurement.

500 The stress regime of the rock volume, by itself, would not have an influence on the $S_{H\max}$ orientation. A rotation
501 of $S_{H\max}$ orientation would primarily be driven by the horizontal differential stresses, i.e., the greater the
502 horizontal differential stresses, the lesser the possibility of any rotation in the $S_{H\max}$ orientation (Bell, 1996a;
503 Yale, 2003; Reiter et al., 2024).

504 The 1 km spatial distance limit can also be confirmed by viewing the $S_{H\max}$ orientation from the boreholes in
505 correlation with their distance from the nearest faults. The TRU1-1 borehole is less than 1 km from the
506 Neuhausen fault. Similarly, the MAR1-1 and RHE1-1 boreholes are closest to the Rheinau fault. The average $S_{H\max}$
507 orientation from the BO, DITF, and HF is $\sim 165^\circ$ along the TRU1-1 borehole, $\sim 175^\circ$ along the MAR1-1 borehole,
508 and $\sim 172.5^\circ$ along the RHE1-1 borehole (Nagra, 2024c, d). Comparing the $S_{H\max}$ orientation values from these
509 three boreholes to the regional $S_{H\max}$ orientation value of $170^\circ \pm 11^\circ$ already strengthens the argument that the
510 faults have minimal effects on $S_{H\max}$ orientation even at a distance of less than 1 km.

511 5.2 Impact of varying fault friction coefficient of the implemented faults

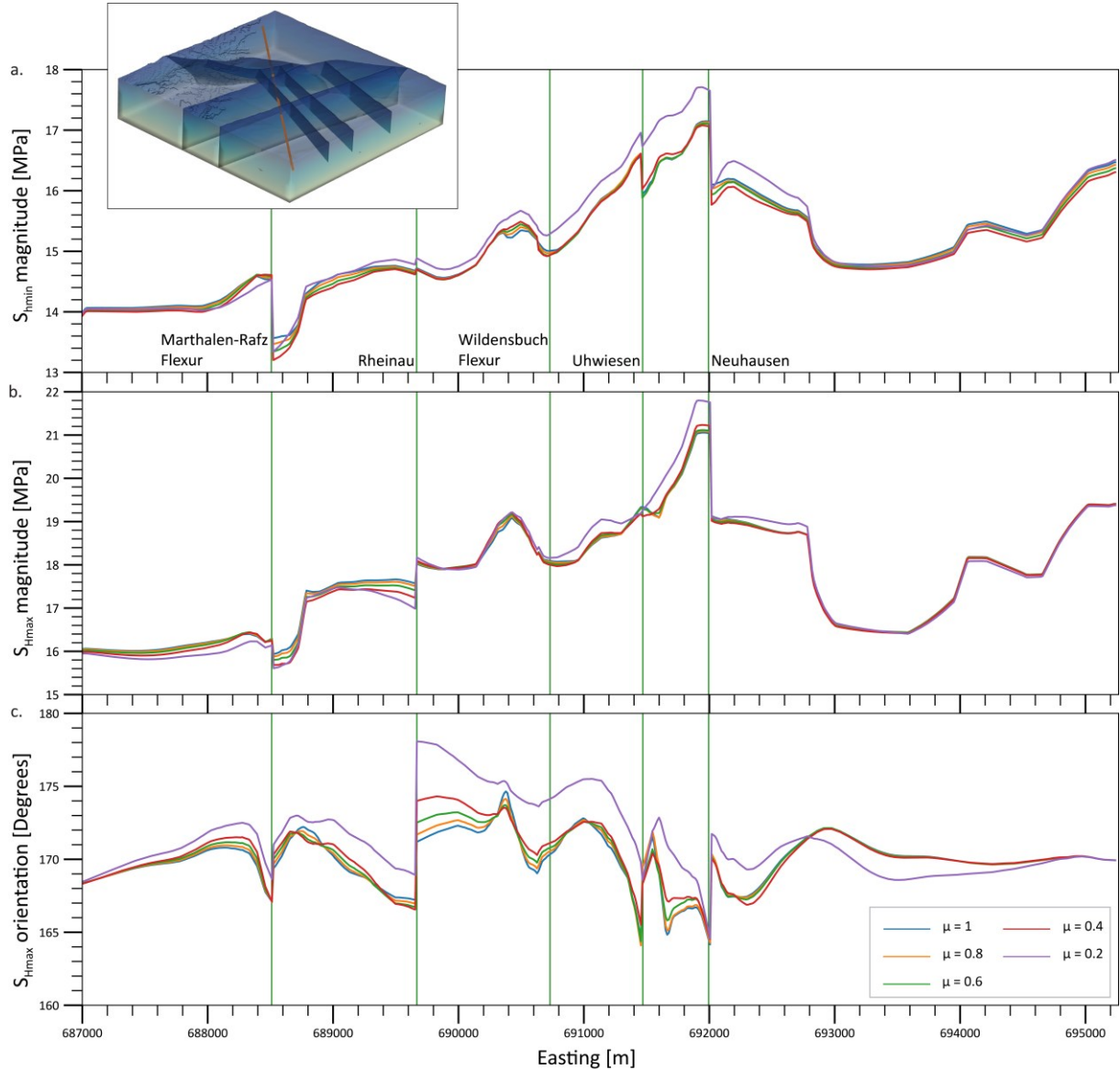
512 In geomechanical modelling, the fault strength is commonly characterized by its friction coefficient (μ) and
513 cohesion (Brandes and Tanner, 2020). In most geological settings, the friction coefficient varies between 0.6 and
514 1.0 in reservoirs with depths where normal stresses are <200 MPa on a pre-existing fracture plane (Byerlee,
515 1978; Zoback and Healy, 1984). In stark contrast, significantly lower friction coefficient values are found in
516 geological settings with extremely weak lithologies, overpressured fault cores, and in faults with very large offset
517 and/or high slip rates (Morrow et al., 1982; Morrow et al., 1992; Di Toro et al., 2011; Hergert et al., 2011; Li et
518 al., 2022). Cohesion varies with different lithologies, but for pre-existing faults, it is commonly assumed to be
519 zero. In general, the value of the friction coefficient varies between 0.4 and 0.8, and is standardly taken as 0.65
520 (Hawkes et al., 2005; Kohli and Zoback, 2013). In northern Switzerland, taking the lithology and the geological
521 setting into consideration, the values of apparent fault friction coefficient also range from 0.6 to 1.0, and very
522 rarely to 0.4 (Kastrup, 2002; Viganò et al., 2021). Kastrup (2002) states that the apparent fault friction value of
523 0.2 is extremely rare in Switzerland and only occurs at depths of more than 10 km.

524 We investigate the effect of varying the friction coefficient of the contact surfaces on the predicted in situ stress
525 state and recalibrate the REF model with a different friction coefficient. The results of stress magnitudes and
526 orientation from friction coefficients 0.2, 0.4, 0.6, and 0.8 are compared to the friction coefficient of 1.0, the
527 value we use in the REF model (Fig. 11). We see that changes in friction coefficient do not significantly affect our
528 model results beyond lateral distances of 1 km. Even within 1 km from the faults, the horizontal stress
529 magnitudes have observable variations of <1 MPa and $<5^\circ$ for the $S_{H\max}$ orientation variations. These variations
530 reduce to <0.25 MPa in both minimum and maximum horizontal stresses, and $<2.5^\circ$ in the $S_{H\max}$ orientation

531 beyond 1 km from the faults. The maximum variations, still far less than the uncertainties in the in situ stress
 532 data of the stress magnitudes and resolvable $S_{H\max}$ orientations, occur at a friction coefficient of 0.2. For the other
 533 values of the friction coefficient, the results are very much comparable to the REF model, with a friction
 534 coefficient of 1. This is to show that changing the friction coefficient has a negligible effect on the predicted
 535 stresses in our model. Minor amounts of slip, in the order of a few tens of cm, occur along the faults in the REF
 536 model during the application of boundary conditions. However, the stress change along the fault due to this slip
 537 is expected to be far less than the much larger background stresses and the differential stresses. Therefore, the
 538 minor slip occurring along the contact surfaces does not influence the overall stress field analysis.

539 These findings are in line with the results from the generic studies by Homberg et al. (1997) and Reiter et al.
 540 (2024), who studied the impact of variable friction coefficient on astress tensor and found that lower values of
 541 friction coefficient lead to a higher stress perturbation near the modelled fault. This is also seen in Fig. 11 and is
 542 because of possible decoupling at the fault and consequently a better dissipation of stress at the faults, facilitated
 543 by lower friction coefficients. The studies also showed that this effect is limited to a distance of 1 km from the
 544 fault zone.

545



546

547 Figure 11: Impact of friction coefficient (μ) on the stress tensor components. The model used here is the REF model. The
 548 results are plotted along the SW-NE horizontal profile at 300 m (b.s.l.), shown in the 3D figure as a red line. Green vertical
 549 lines with the respective fault names denote the location where the profile crosses the modelled faults.

550 5.3 Dependence of the modeling results on fault implementation

551 Faults in the REF model are represented as contact surfaces, a common and effective approach for large-scale
552 geomechanical simulations. Using contact elements to model faults seems to be a reasonable simplification for
553 large, field-scale reservoir models, where the actual width of the fault core is much smaller than the overall size
554 of the model. Hence, contact surfaces are computationally efficient for reservoir-scale models where actual fault
555 zone widths are negligible compared to model dimensions (Caine et al., 1996; Treffeisen and Henk, 2020). Since
556 our interest is on reservoir scale, alternative fault representation using, e.g. continuous rectangular finite
557 element grid, or a continuous curvilinear finite element grid in a homogenized continuum (Henk, 2009, 2020) is
558 not used in our study. Furthermore, the results from Treffeisen and Henk (2020) and Reiter et al. (2024) show
559 that the stress and strain perturbations from different technical fault implementations vary only within a few
560 tens to a few hundred meters from the fault representation. As we focus only on the far-field stress state, it can
561 be safely assumed that the choice of fault implementation approach does not significantly affect the far-field
562 results.

563 Although a numerical value does not exist for what is universally defined as far-field stresses, our model indicates
564 that at a distance of >500 m from the faults, the impact of the faults on the stress field is clearly smaller than the
565 uncertainty of the model itself and smaller than the expected variability of the stress field. As seen in Fig. 10, the
566 influence of faults on the stress field is limited to within 1 km from the contact surfaces. Beyond this distance,
567 the choice of the fault representation approach would have no significant impact on the predicted in situ stress
568 state.

569 5.4 Limitations of the study's results and future outlook

570 In the REF model, the faults, represented by contact surfaces, are simplified and a unified representation of
571 numerous small fault patches that were interpreted from the 3D seismic interpretation. This simplification is
572 necessary for an easier and reasonable representation of fault structures and the consequent computational
573 simulation feasibility of the model. However, the reality is more complex. In the subsurface, faults often occur in
574 clusters and display heterogeneous geometry, composition, and structure (Tanner and Brandes, 2020). Large
575 faults are often accompanied by zones of secondary faults, which can extend the spatial influence of faults on
576 the stress state. Small fault segments of the primary fault and the associated secondary faults can lead to a higher
577 stress concentration along the fault surfaces, complicating the interaction between faults and the in situ stresses
578 (Jones, 1988; Maerten et al., 2002). A single fault may also have complex geometry with multiple bends (Saucier
579 et al., 1992; Roche et al., 2021), increasing its influence on stresses compared to the planar faults.

580 Our study focuses on a reservoir scale, in the order of a few km, to predict present day stress variation in the
581 area of interest. While seven faults were implemented in the REF model, many more fractures or joints exist in
582 reality but cannot be resolved at our current lateral resolution of approximately 70–100 m, and the available
583 structural geological data. Including these would significantly increase the element count and computational
584 demand, far beyond the scope or need of most studies. It is important to emphasize that the focus of our results
585 is only the far-field present day stresses, and in an intact and undisturbed rock volume.

586 While previous studies have documented significant stress rotations near fault tips, they also emphasize that
587 these perturbations are typically localized, rarely extending beyond a few hundred meters from the termination
588 point (Homberg et al., 1997; Nicol et al., 2020). Our findings are in general agreement with this observation. In
589 our model, fault tips ending within the Mesozoic sediments indeed exhibit localized stress concentrations and
590 enhanced stress rotations. However, because these effects are spatially restricted, they do not significantly alter
591 the regional stress field predicted by the fault-agnostic models at distances greater than a few 100 m from the
592 structural discontinuities.

593 Extreme cases exist where large-scale faulting separated the crust into distinct fault blocks, each having an
594 independent $S_{H\max}$ orientation between adjacent fault blocks of the same field (Yale et al., 1994; Yale and Ryan,
595 1994; Bell, 1996b; Kattenhorn et al., 2000; Hergert and Heidbach, 2011; Hergert et al., 2011; Li et al., 2019; Qin
596 et al., 2024). While complex stress patterns and large $S_{H\max}$ rotations have been reported for major fault systems
597 such as the Møre–Trøndelag Fault Complex and the San Andreas Fault, these systems differ fundamentally from
598 the Alpine Foreland Basin in terms of tectonic setting, fault displacement magnitude, and fault frictional

599 properties (Zoback et al., 1987; Pascal and Gabrielsen, 2001; Roberts and Myrvang, 2004). In particular, the large
600 offsets and anomalously low friction coefficients reported for these systems are not representative of the fault
601 conditions in northern Switzerland. But, as seen in our study region, if the Mesozoic sediments are not massively
602 faulted or fractured, have sufficiently large differential stresses, and are located in an intraplate Foreland Basin
603 setting, it could be expected that the impact of faults on the stress state would only be within 1 km from the
604 fault zone. However, further investigation is needed for other geological settings, with different lithologies such
605 as salt domes, anhydrite, or crystalline rock formations, or regions where faults exhibit more complex geometry
606 with more curvature/ bends, or with extremely large total offsets and high slip rates, to confirm the broader
607 applicability of our results.

608 6. Conclusion

609 We evaluated the influence of faults on the regional stress state using 3D geomechanical models of the Zürich
610 Nordost siting region, which are calibrated on a robust dataset of 30 minimum horizontal and 15 maximum
611 horizontal stress magnitudes from two boreholes. We directly compare the predicted stress states between
612 models where faults have been modelled as contact surfaces and models where faults have been excluded or
613 mechanically deactivated. Our findings show that faults cause only local stress perturbations, within 500 m from
614 the contact surfaces, with their impact becoming negligible beyond 1 km from the fault. At this scale, stress
615 variations are mainly controlled by contrasts in rock stiffness on the juxtaposed formations rather than just the
616 relative mechanical weakness presented by the fault plane. The variations between the model realizations must
617 also be viewed in conjunction with the rock stress variability, which in turn results from stiffness variability. The
618 fault-induced stress effects at distances >1 km are smaller than the typical resolution limits of stress data and
619 uncertainties of the stress magnitude measurements, which are $\pm 11^\circ$ for $S_{H\max}$ orientation and 0.7–3.5 MPa for
620 stress magnitude, derived from the description of stress magnitudes as ranges. Importantly, omitting faults from
621 the modeling workflow can reduce model setup and computational time from months to 1–2 days using
622 alternative discretization strategies, without sacrificing stress prediction reliability. These findings provide
623 valuable guidance for efficient and reliable reservoir-scale geomechanical modeling, including site assessments
624 for a deep geological repository, where predicting far-field in situ stresses in intact rock volumes is essential,
625 given that the storage sites are located away from active faults (>1 km) in an intact and undisturbed rock volume.
626 However, further studies in different geologic settings and under different stress conditions are required to verify
627 the general applicability of our results from northern Switzerland.

628 Author contribution

629 LSARV: Conceptualization, Formal analysis, Methodology, Model preparation, Validation, Visualization, Writing
630 (original draft preparation), and Writing (review and editing).

631 OH: Conceptualization, Data curation, Funding acquisition, Project administration, Resources, Supervision,
632 Validation, and Writing (review and editing).

633 MZ: Resources, Software, Supervision, Validation, and Writing (review and editing).

634 KR: Methodology, Resources, Model preparation, Validation, and Writing (review and editing), Funding
635 acquisition.

636 AH: Funding acquisition, Project administration, and Writing (review and editing).

637 MR: Conceptualization, Visualization, Writing (review and editing).

638 SBG: Resources, and Writing (review and editing).

639 TH: Visualization, Writing (review and editing).

640 Competing interests

641 The authors declare that they have no conflict of interest.

642 Disclaimer

643 Publisher's note: Copernicus Publications remains neutral with regard to jurisdictional claims made in the text,
644 published maps, institutional affiliations, or any other geographical representation in this paper. While
645 Copernicus Publications makes every effort to include appropriate place names, the final responsibility lies with
646 the authors.

647 Acknowledgements

648 We thank NAGRA for providing access to the extensive dataset used in our study. We also thank SQuaRe and
649 SpannEnd 2.0 for the funding.

650 Financial support

651 The authors gratefully acknowledge the funding provided by the Bundesministerium für Umwelt, Naturschutz,
652 nukleare Sicherheit und Verbraucherschutz through the project SQuaRe (project number: 02E12062B), and by
653 the Bundesgesellschaft für Endlagerung (BGE) through the project SpannEnD 2.0 (<https://www.spannend-projekt.de>). Additional support was provided by the National Cooperative for the Disposal of Radioactive Waste
654 (Nagra), Switzerland.

655 References

656 Ahlers, S., Henk, A., Hergert, T., Reiter, K., Müller, B., Röckel, L., Heidbach, O., Morawietz, S., Scheck-
657 Wenderoth, M., and Anikiev, D.: 3D crustal stress state of Germany according to a data-calibrated geomechanical
658 model, *Solid Earth*, 12, 1777–1799, <https://doi.org/10.5194/se-12-1777-2021>, 2021.

659 Ahlers, S., Röckel, L., Hergert, T., Reiter, K., Heidbach, O., Henk, A., Müller, B., Morawietz, S., Scheck-
660 Wenderoth, M., and Anikiev, D.: The crustal stress field of Germany: a refined prediction, *Geothermal Energy*,
661 10, 10, <https://doi.org/10.1186/s40517-022-00222-6>, 2022.

662 Aleksandrowski, P., Inderhaug, O. H. E., and Knapstad, B.: Tectonic structures and wellbore breakout orientation,
663 The 33rd U.S. Symposium on Rock Mechanics (USRMS), Santa Fe, New Mexico, USA, 3–5 June,
664 [https://doi.org/10.1016/0148-9062\(93\)90652-T](https://doi.org/10.1016/0148-9062(93)90652-T), 1992.

665 Amadei, B. and Stephansson, O.: Rock stress and its measurement, Springer Dordrecht,
666 <https://doi.org/10.1007/978-94-011-5346-1>, 1997.

667 Azzola, J., Valley, B., Schmittbuhl, J., and Genter, A.: Stress characterization and temporal evolution of borehole
668 failure at the Rittershoffen geothermal project, *Solid Earth*, 10, 1155–1180, <https://doi.org/10.5194/se-10-1155-2019>, 2019.

669 Barton, C. A. and Zoback, M. D.: Stress perturbations associated with active faults penetrated by boreholes:
670 Possible evidence for near-complete stress drop and a new technique for stress magnitude measurement, *Journal of Geophysical Research: Solid Earth*, 99, 9373–9390, <https://doi.org/10.1029/93JB03359>, 1994.

671 Bell, J. S.: Petro Geoscience 1. In situ stresses in sedimentary rocks (Part 1): Measurement Techniques, *Geoscience
672 Canada*, 23, 1996a.

673 Bell, J. S.: Petro Geoscience 2. In-Situ Stresses in Sedimentary Rocks (Part 2): Application of Stress
674 Measurements, *Geoscience Canada*, 23, 135–153, 1996b.

675 Bell, J. S. and Gough, D. I.: Northeast-southwest compressive stress in Alberta evidence from oil wells, *Earth and
676 Planetary Science Letters*, 45, 475–482, [https://doi.org/10.1016/0012-821X\(79\)90146-8](https://doi.org/10.1016/0012-821X(79)90146-8), 1979.

677 Bell, J. S. and Grasby, S. E.: The stress regime of the Western Canadian Sedimentary Basin, *Geofluids*, 12, 150–
678 165, <https://doi.org/10.1111/j.1468-8123.2011.00349.x>, 2012.

682 Bérard, T. and Desroches, J.: Geological structure, geomechanical perturbations, and variability in hydraulic
683 fracturing performance at the scale of a square mile, *Geomechanics for Energy and the Environment*, 26, 100137,
684 <https://doi.org/10.1016/j.gete.2019.100137>, 2021.

685 Berard, T., Sinha, B. K., Van Ruth, P., Dance, T., John, Z., and Tan, C.: Stress estimation at the Otway CO2
686 storage site, Australia, *SPE Asia Pacific Oil and Gas Conference and Exhibition*, Perth, Australia,
687 <https://doi.org/10.2118/116422-MS>, 2008.

688 Boness, N. L. and Zoback, M. D.: A multiscale study of the mechanisms controlling shear velocity anisotropy in
689 the San Andreas Fault Observatory at Depth, *GEOPHYSICS*, 71, F131–F146, <https://doi.org/10.1190/1.2231107>,
690 2006.

691 Brandes, C. and Tanner, D. C.: Chapter 2 - Fault mechanics and earthquakes, in: *Understanding Faults*, edited by:
692 Tanner, D., and Brandes, C., Elsevier, 11–80, <https://doi.org/10.1016/B978-0-12-815985-9.00002-3>, 2020.

693 Brodsky, E. E., Mori, J. J., Anderson, L., Chester, F. M., Conin, M., Dunham, E. M., Eguchi, N., Fulton, P. M.,
694 Hino, R., Hirose, T., Ikari, M. J., Ishikawa, T., Jeppson, T., Kano, Y., Kirkpatrick, J., Kodaira, S., Lin, W.,
695 Nakamura, Y., Rabinowitz, H. S., Regalla, C., Remitti, F., Rowe, C., Saffer, D. M., Saito, S., Sample, J., Sanada,
696 Y., Savage, H. M., Sun, T., Toczko, S., Ujiie, K., Wolfson-Schwehr, M., and Yang, T.: The State of Stress on the
697 Fault Before, During, and After a Major Earthquake, *Annual Review of Earth and Planetary Sciences*, 48, 49–74,
698 <https://doi.org/10.1146/annurev-earth-053018-060507>, 2020.

699 Brooke-Barnett, S., Flottmann, T., Paul, P. K., Busetti, S., Hennings, P., Reid, R., and Rosenbaum, G.: Influence
700 of basement structures on in situ stresses over the Surat Basin, southeast Queensland, *Journal of Geophysical
701 Research: Solid Earth*, 120, 4946–4965, <https://doi.org/10.1002/2015JB011964>, 2015.

702 Brudy, M., Fuchs, K., and Zoback, M. D.: Stress orientation profile to 6 km depth in the KTB main borehole, KTB
703 Report 93-2: Contributions to the 6. Annual KTB-Colloquium, *Geoscientific Results*, Giessen, Germany, 1–2 June,
704 195–197, <https://doi.org/10.2312/KTB.93-2>, 1992.

705 Brudy, M., Zoback, M. D., Fuchs, K., Rummel, F., and Baumgärtner, J.: Estimation of the complete stress tensor
706 to 8 km depth in the KTB scientific drill holes: Implications for crustal strength, *Journal of Geophysical Research:
707 Solid Earth*, 102, 18453–18475, <https://doi.org/10.1029/96JB02942>, 1997.

708 Buchmann, T. J. and Connolly, P. T.: Contemporary kinematics of the Upper Rhine Graben: A 3D finite element
709 approach, *Global and Planetary Change*, 58, 287–309, <https://doi.org/10.1016/j.gloplacha.2007.02.012>, 2007.

710 Burkhard, M. and Sommaruga, S.: Evolution of the western Swiss Molasse basin: structural relations with the Alps
711 and the Jura belt, *Geological Society, London, Special Publications*, 134, 279–298,
712 <https://doi.org/10.1144/GSL.SP.1998.134.01.13>, 1998.

713 Byerlee, J.: Friction of rocks, *pure and applied geophysics*, 116, 615–626, <https://doi.org/10.1007/BF00876528>,
714 1978.

715 Caine, J. S., Evans, J. P., and Forster, C. B.: Fault zone architecture and permeability structure, *Geology*, 24, 1025–
716 1028, [https://doi.org/10.1130/0091-7613\(1996\)024%3C1025:FZAAPS%3E2.3.CO;2](https://doi.org/10.1130/0091-7613(1996)024%3C1025:FZAAPS%3E2.3.CO;2), 1996.

717 Catalli, F., Meier, M.-A., and Wiemer, S.: The role of Coulomb stress changes for injection-induced seismicity:
718 The Basel enhanced geothermal system, *Geophysical Research Letters*, 40, 72–77,
719 <https://doi.org/10.1029/2012GL054147>, 2013.

720 Chéry, J., Zoback, M. D., and Hickman, S.: A mechanical model of the San Andreas fault and SAFOD Pilot Hole
721 stress measurements, *Geophysical Research Letters*, 31, <https://doi.org/10.1029/2004GL019521>, 2004.

722 Cloetingh, S., Cornu, T., Ziegler, P. A., and Beekman, F.: Neotectonics and intraplate continental topography of
723 the northern Alpine Foreland, *Earth-Science Reviews*, 74, 127–196,
724 <https://doi.org/10.1016/j.earscirev.2005.06.001>, 2006.

725 Cloetingh, S. and Wortel, R.: Regional stress field of the Indian Plate, *Geophysical Research Letters*, 12, 77–80,
726 <https://doi.org/10.1029/GL012i002p00077>, 1985.

727 Coward, M. and Dietrich, D.: Alpine tectonics — an overview, Geological Society, London, Special Publications, 728 45, 1–29, <https://doi.org/10.1144/GSL.SP.1989.045.01.0>, 1989.

729 Desroches, J., Peyret, E., Gisolf, A., Wilcox, A., Di Giovanni`i, M., de Jong, A. S., Sepehri, S., Garrard, R., and 730 Giger, S.: Stress Measurement Campaign in Scientific Deep Boreholes: Focus on Tools and Methods, *Petrophysics* 731 - The SPWLA Journal, 64, 621–639, <https://doi.org/10.30632/PJV64N5-2023a2>, 2023.

732 Desroches, J., Peyret, E., Gisolf, A., Wilcox, A., Di Giovanni, M., de Jong, A. S., Sepehri, S., Garrard, R., and 733 Giger, S.: Stress Measurement Campaign in Scientific Deep Boreholes: Focus on Tool and Methods, *SPWLA* 734 62nd Annual Logging Symposium, Virtual Event, 17–20 May, <https://doi.org/10.30632/SPWLA-2021-0056>, 735 2021a.

736 Desroches, J., Peyret, E., Gisolf, A., Wilcox, A., Di Giovanni, M., Schram de Jong, A., Milos, B., Gonus, J., 737 Bailey, E., Sepehri, S., Garitte, B., Garrard, R., and Giger, S.: Stress-Measurement Campaign in Scientific Deep 738 Boreholes: From Planning to Interpretation, 55th U.S. Rock Mechanics/Geomechanics Symposium, Virtual Event, 739 20–23 June, 2021b.

740 Di Toro, G., Han, R., Hirose, T., De Paola, N., Nielsen, S., Mizoguchi, K., Ferri, F., Cocco, M., and Shimamoto, 741 T.: Fault lubrication during earthquakes, *Nature*, 471, 494–498, <https://doi.org/10.1038/nature09838>, 2011.

742 Diebold, P. and Noack, T.: Late Palaeozoic troughs and Tertiary structures in the eastern Folded Jura, in: *Deep* 743 *Structure of the Swiss Alps: Results of NRP20*, edited by: Pfiffner, O. A., Lehner, P., Heitzmann, P., Mueller, S., 744 and Steck, A., Birkhäuser Verlag, Basel, 59–63, 1997.

745 Fiebig, M. and Preusser, F.: Pleistocene glaciations of the northern Alpine Foreland, *Geographica Helvetica*, 63, 746 145–150, <https://doi.org/10.5194/gh-63-145-2008>, 2008.

747 Fischer, K. and Henk, A.: A workflow for building and calibrating 3-D geomechanical models- a case study for a 748 gas reservoir in the North German Basin, *Solid Earth*, 4, 347–355, <https://doi.org/10.5194/se-4-347-2013>, 2013.

749 Gens, A., Garitte, B., Olivella, S., and Vaunat, J.: Applications of multiphysical geomechanics in underground 750 nuclear waste storage, *European Journal of Environmental and Civil Engineering*, 13, 7–8, 751 <https://doi.org/10.1080/19648189.2009.9693162>, 2009.

752 Gorin, G., Signer, C., and Amberger, G.: Structural configuration of the western Swiss Molasse Basin as defined 753 by reflection seismic data, *Eclogae Geologicae Helvetiae*, 86, 693–716, 1993.

754 Gough, D. I. and Bell, J. S.: Stress orientations from borehole wall fractures with examples from Colorado, east 755 Texas, and northern Canada, *Canadian Journal of Earth Sciences*, 19, 1358–1370, <https://doi.org/10.1139/e82-118>, 756 1982.

757 Hawkes, C., McLellan, P., and Bachu, S.: Geomechanical factors affecting geological storage of CO₂ in depleted 758 oil and gas reservoirs, *Journal of Canadian Petroleum Technology*, 44, 2005.

759 Heidbach, O., Rajabi, M., Cui, X., Fuchs, K., Müller, B., Reinecker, J., Reiter, K., Tingay, M., Wenzel, F., Xie, 760 F., Ziegler, M. O., Zoback, M.-L., and Zoback, M.: The World Stress Map database release 2016: Crustal stress 761 pattern across scales, *Tectonophysics*, 744, 484–498, <https://doi.org/10.1016/j.tecto.2018.07.007>, 2018.

762 Heidbach, O., Rajabi, M., Di Giacomo, D., Harris, J., Lammers, S., Morawietz, S., Pierdominici, S., Reiter, K., 763 Storchak, D., von Specht, S., and Ziegler, M. O.: World Stress Map Database Release 2025, 764 <https://doi.org/10.5880/WSM.2025.001>, 2025a.

765 Heidbach, O., Reinecker, J., Diehl, T., Desroches, J., Ziegler, M. O., Reiter, K., Vietor, T., and Giger, S. B.: The 766 present-day crustal stress field of the Molasse Basin in Switzerland, *Swiss Journal of Geosciences*, 767 <https://doi.org/10.1186/s00015-025-00487-6>, 2025b.

768 Heidbach, O., Reinecker, J., Tingay, M., Müller, B., Sperner, B., Fuchs, K., and Wenzel, F.: Plate boundary forces 769 are not enough: Second- and third-order stress patterns highlighted in the World Stress Map database, *Tectonics*, 770 26, TC6014, <https://doi.org/10.1029/2007TC002133>, 2007.

771 Henk, A.: Pre-drilling prediction of the tectonic stress field with geomechanical models, *First Break*, 23, 53–57,
772 <https://doi.org/10.3997/1365-2397.2005021>, 2005.

773 Henk, A.: Perspectives of Geomechanical Reservoir Models - Why Stress is Important, *Oil Gas European*
774 Magazine, 35(1), 20–24, 2009.

775 Henk, A.: Chapter 4 - Numerical modelling of faults, in: *Understanding Faults*, edited by: Tanner, D., and Brandes,
776 C., Elsevier, 147–165, <https://doi.org/10.1016/B978-0-12-815985-9.00004-7>, 2020.

777 Hergert, T. and Heidbach, O.: Geomechanical model of the Marmara Sea region—II. 3-D contemporary
778 background stress field, *Geophysical Journal International*, 185, 1090–1102, <https://doi.org/10.1111/j.1365-246X.2011.04992.x>, 2011.

780 Hergert, T., Heidbach, O., Bécel, A., and Laigle, M.: Geomechanical model of the Marmara Sea region - I. 3-D
781 contemporary kinematics, *Geophysical Journal International*, 185, 1073–1089, <https://doi.org/10.1111/j.1365-246X.2011.04991.x>, 2011.

783 Hergert, T., Heidbach, O., Reiter, K., Giger, S. B., and Marschall, P.: Stress field sensitivity analysis in a
784 sedimentary sequence of the Alpine foreland, northern Switzerland, *Solid Earth*, 6, 533–552,
785 <https://doi.org/10.5194/se-6-533-2015>, 2015.

786 Hickman, S. and Zoback, M.: Stress orientations and magnitudes in the SAFOD pilot hole, *Geophysical Research*
787 Letters, 31, <https://doi.org/10.1029/2004GL020043>, 2004.

788 Homberg, C., Hu, J. C., Angelier, J., Bergerat, F., and Lacombe, O.: Characterization of stress perturbations near
789 major fault zones: insights from 2-D distinct-element numerical modelling and field studies (Jura mountains),
790 *Journal of Structural Geology*, 19, 703–718, [https://doi.org/10.1016/S0191-8141\(96\)00104-6](https://doi.org/10.1016/S0191-8141(96)00104-6), 1997.

791 Illies, J. H.: The Rhine graben rift system-plate tectonics and transform faulting, *Geophysical surveys*, 1, 27–60,
792 <https://doi.org/10.1007/BF01449550>, 1972.

793 Jaeger, J. C., Cook, N. G. W., and Zimmerman, R. W.: *Fundamentals of Rock Mechanics*, 4, Blackwell Publishing,
794 2007.

795 Jo, Y., Chang, C., Ji, S.-H., and Park, K.-W.: In situ stress states at KURT, an underground research laboratory in
796 South Korea for the study of high-level radioactive waste disposal, *Engineering Geology*, 259, 105198,
797 <https://doi.org/10.1016/j.enggeo.2019.105198>, 2019.

798 Jones, W. B.: Listric growth faults in the Kenya Rift Valley, *Journal of Structural Geology*, 10, 661–672,
799 [https://doi.org/10.1016/0191-8141\(88\)90074-0](https://doi.org/10.1016/0191-8141(88)90074-0), 1988.

800 Jordan, P.: Triassic. Basin evolution: Switzerland., in: *The Geology of Central Europe. Volume 2: Mesozoic and*
801 *Cenozoic*, edited by: McCann, T., Geological Society of London, London, 785–788,
802 <https://doi.org/10.1144/CEV2P>, 2008.

803 Kastrup, U.: Seismotectonics and Stress Field Variations in Switzerland, Dissertation, Swiss Federal Institute of
804 Technology Zurich (ETH Zurich), Zurich, 162 pp., <https://doi.org/10.3929/ethz-a-004423062>, 2002.

805 Kattenhorn, S. A., Aydin, A., and Pollard, D. D.: Joints at high angles to normal fault strike: an explanation using
806 3-D numerical models of fault-perturbed stress fields, *Journal of Structural Geology*, 22, 1–23,
807 [https://doi.org/10.1016/S0191-8141\(99\)00130-3](https://doi.org/10.1016/S0191-8141(99)00130-3), 2000.

808 Kempf, O. and Adrian, P., O.: Early Tertiary evolution of the North Alpine Foreland Basin of the Swiss Alps and
809 adjoining areas, *Basin Research*, 16, 549–567, <https://doi.org/10.1111/j.1365-2117.2004.00246.x>, 2004.

810 Kingsborough, R. H., Williams, A. F., and Hillis, R. R.: Borehole Instability on the Northwest Shelf of Australia,
811 SPE Asia-Pacific Conference, Perth, Australia, 4–7 Nov, <https://doi.org/10.2118/23015-MS>, 1991.

812 Kohli, A. H. and Zoback, M. D.: Frictional properties of shale reservoir rocks, *Journal of Geophysical Research: Solid Earth*, 118, 5109–5125, <https://doi.org/10.1002/jgrb.50346>, 2013.

814 Laubscher, H.: Jura, Alps and the boundary of the Adria subplate, *Tectonophysics*, 483, 223–239,
815 <https://doi.org/10.1016/j.tecto.2009.10.011>, 2010.

816 Lecampion, B. and Lei, T.: Reconstructing the 3D Initial Stress State over Reservoir Geomechanics Model from
817 Local Measurements and Geological Priors: A Bayesian Approach, *Schlumberger J. of Modeling, Design and*
818 *Simulation*, 1, 100–104, <https://infoscience.epfl.ch/handle/20.500.14299/119734>, 2010.

819 Li, P., Cai, M.-f., Miao, S.-j., and Guo, Q.-f.: New Insights Into The Current Stress Field Around the Yishu Fault
820 Zone, Eastern China, *Rock Mechanics and Rock Engineering*, 52, 4133–4145, <https://doi.org/10.1007/s00603-019-01792-x>, 2019.

822 Li, X., Hergert, T., Henk, A., and Zeng, Z.: Contemporary background stress field in the eastern Tibetan Plateau:
823 Insights from 3D geomechanical modeling, *Tectonophysics*, 822, 229177,
824 <https://doi.org/10.1016/j.tecto.2021.229177>, 2022.

825 Long, J. C. S. and Ewing, R. C.: YUCCA MOUNTAIN: Earth-Science Issues at a Geologic Repository for High-
826 Level Nuclear Waste, *Annual Review of Earth and Planetary Sciences*, 32, 363–401,
827 <https://doi.org/10.1146/annurev.earth.32.092203.122444>, 2004.

828 Madritsch, H., Looser, N., Schneeberger, R., Wohlwend, S., Guillong, M., and Malz, A.: Reconstructing the
829 Evolution of Foreland Fold-And-Thrust Belts Using U-Pb Calcite Dating: An Integrated Case-Study From the
830 Easternmost Jura Mountains (Switzerland), *Tectonics*, 43, e2023TC008181,
831 <https://doi.org/10.1029/2023TC008181>, 2024.

832 Maerten, L., Gillespie, P., and Pollard, D. D.: Effects of local stress perturbation on secondary fault development,
833 *Journal of Structural Geology*, 24, 145–153, [https://doi.org/10.1016/S0191-8141\(01\)00054-2](https://doi.org/10.1016/S0191-8141(01)00054-2), 2002.

834 Mao, J.: A finite element approach to solve contact problems in geotechnical engineering, *International Journal
835 for Numerical and Analytical Methods in Geomechanics*, 29, 525–550, <https://doi.org/10.1002/nag.424>, 2005.

836 Marchant, R., Ringgenberg, Y., Stampfli, G., Birkhäuser, P., Roth, P., and Meier, B.: Paleotectonic evolution of
837 the Zürcher Weinland (northern Switzerland), based on 2D and 3D seismic data, *Eclogae Geologicae Helvetiae*,
838 98, 345–362, <https://doi.org/10.1007/s00015-005-1171-8>, 2005.

839 McCann, T., Pascal, C., Timmerman, M. J., Krzywiec, P., López-Gómez, J., Wetzel, L., Krawczyk, C. M., Rieke,
840 H., and Lamarche, J.: Post-Variscan (end Carboniferous-Early Permian) basin evolution in Western and Central
841 Europe, *Geological Society, London, Memoirs*, 32, 355–388, <https://doi.org/10.1144/GSL.MEM.2006.032.01.22>,
842 2006.

843 Morrow, C., Radney, B., and Byerlee, J.: Chapter 3 Frictional Strength and the Effective Pressure Law of
844 Montmorillonite and Illite Clays, in: *International Geophysics*, edited by: Evans, B., and Wong, T.-f., Academic
845 Press, 69–88, [https://doi.org/10.1016/S0074-6142\(08\)62815-6](https://doi.org/10.1016/S0074-6142(08)62815-6), 1992.

846 Morrow, C., Shi, L., and Byerlee, J.: Strain hardening and strength of clay-rich fault gouges, *Journal of
847 Geophysical Research: Solid Earth*, 87, 6771–6780, <https://doi.org/10.1029/JB087iB08p06771>, 1982.

848 Nagra: Erläuterungen zur Geologischen Karte der zentralen Nordschweiz 1:100 000, NAGRA, Baden,
849 Switzerland, NAGRA Technischer Bericht NTB 84-25, 263 pp., 1984.

850 Nagra: Zur Tektonik der zentralen Nordschweiz - Interpretation aufgrund regionaler Seismik, Oberflächengeologie
851 und Tiefbohrungen, NAGRA, Wettingen, Switzerland, NAGRA Technischer Bericht NTB 90-04, 277 pp., 1991.

852 Nagra: 3D-Seismik: Räumliche Erkundung der mesozoischen Sedimentschichten im Zürcher Weinland, NAGRA,
853 Switzerland, NAGRA Technischer Bericht NTB 00-03, 180 pp., 2001.

854 Nagra: Geologische Entwicklung der Nordschweiz, Neotektonik und Langzeitszenarien Zürcher Weinland,
855 NAGRA, Wettingen, Switzerland, NAGRA Technischer Bericht NTB 99-08, 257 pp., 2002a.

856 Nagra: Projekt Opalinuston: Synthese der geowissenschaftlichen Untersuchungsergebnisse Entsorgungsnachweis
857 für abgebrannte Brennelemente, verglaste hochaktive sowie langlebige mittelaktive Abfälle, NAGRA, Wettingen,
858 Switzerland, NAGRA Technischer Bericht NTB 02-03, 714 pp., 2002b.

859 Nagra: Vorschlag geologischer Standortgebiete für das SMA-und das HAA-Lager, NAGRA, Wettingen,
860 Switzerland, NAGRA Technischer Bericht NTB 08-04, 477 pp., 2008.

861 Nagra: Analyse des rezenten Spannungsfelds der Nordschweiz, NAGRA, Wettingen, Switzerland, NAGRA
862 Arbeitsbericht NAB 12-05, 146 pp., 2013.

863 Nagra: Tektonische Karte des Nordschweizer Permokarbontrags: Aktualisierung basierend auf 2D-Seismik und
864 Schweredaten, NAGRA, Wettingen, Switzerland, NAGRA Arbeitsbericht NAB 14-17, 64 pp., 2014.

865 Nagra: 3D Seismic Interpretation of Stratigraphic Horizons and Structures in Time Domain, NAGRA, Wettingen,
866 Switzerland, NAGRA Arbeitsbericht NAB 23-19, 151 pp., 2024a.

867 Nagra: Geological Properties of the Jura Ost, Nördlich Lägern and Zürich Nordost Siting Regions for Safety
868 Assessment, NAGRA, Wettingen, Switzerland, NAGRA Arbeitsbericht NAB 24-10 Rev. 1, 44 pp., 2024b.

869 Nagra: Geosynthesis of Northern Switzerland, NAGRA, Wettingen, Switzerland, NAGRA Technischer Bericht
870 NTB 24-17, 604 pp., 2024c.

871 Nagra: In-Situ Stress Field in the Siting Regions Jura Ost, Nördlich Lägern and Zürich Nordost, NAGRA,
872 Wettingen, Switzerland, NAGRA Arbeitbericht NAB 24-19, 131 pp., 2024d.

873 Nicol, A., Walsh, J., Childs, C., and Manzocchi, T.: Chapter 6 - The growth of faults, in: Understanding Faults,
874 edited by: Tanner, D., and Brandes, C., Elsevier, 221–255, <https://doi.org/10.1016/B978-0-12-815985-9.00006-0>,
875 2020.

876 Pascal, C. and Gabrielsen, R. H.: Numerical modeling of Cenozoic stress patterns in the mid-Norwegian margin
877 and the northern North Sea, *Tectonics*, 20, 585–599, <https://doi.org/10.1029/2001TC900007>, 2001.

878 Pijnenburg, R. P. J., Verberne, B. A., Hangx, S. J. T., and Spiers, C. J.: Inelastic Deformation of the Slochteren
879 Sandstone: Stress-Strain Relations and Implications for Induced Seismicity in the Groningen Gas Field, *Journal*
880 *of Geophysical Research: Solid Earth*, 124, 5254–5282, <https://doi.org/10.1029/2019JB017366>, 2019.

881 Preusser, F., Graf, H. R., Keller, O., Krayss, E., and Schlüchter, C.: Quaternary glaciation history of northern
882 Switzerland, *E&G Quaternary Sci. J.*, 60, 21, <https://doi.org/10.3285/eg.60.2-3.06>, 2011.

883 Qin, X., Zhao, X., Zhang, C., Li, P., Chen, Q., and Wang, J.: Measurement and Assessment of the In-Situ Stress
884 of the Shazaoyuan Rock Block, a Candidate Site for HLW Disposal in Northwest China, *Rock Mechanics and*
885 *Rock Engineering*, 57, 4011–4031, <https://doi.org/10.1007/s00603-024-03775-z>, 2024.

886 Rajabi, M., Heidbach, O., Tingay, M., and Reiter, K.: Prediction of the present-day stress field in the Australian
887 continental crust using 3D geomechanical–numerical models, *Australian Journal of Earth Sciences*, 64, 435–454,
888 <https://doi.org/10.1080/08120099.2017.1294109>, 2017a.

889 Rajabi, M., Tingay, M., and Heidbach, O.: The present-day state of tectonic stress in the Darling Basin, Australia:
890 Implications for exploration and production, *Marine and Petroleum Geology*, 77, 776–790,
891 <https://doi.org/10.1016/j.marpetgeo.2016.07.021>, 2016.

892 Rajabi, M., Tingay, M., Heidbach, O., Hillis, R., and Reynolds, S.: The present-day stress field of Australia, *Earth-*
893 *Science Reviews*, 168, 165–189, <https://doi.org/10.1016/j.earscirev.2017.04.003>, 2017b.

894 Rajabi, M., Tingay, M., Heidbach, O., and King, R.: The Role of Faults and Fractures in Local and Regional
895 Perturbation of Present-day Horizontal Stresses - An Example from the Clarence-Moreton Basin, Eastern
896 Australia, 2015, 1–5, <https://doi.org/10.3997/2214-4609.201413346>, 2015.

897 Rajabi, M., Tingay, M., King, R., and Heidbach, O.: Present-day stress orientation in the Clarence-Moreton Basin
898 of New South Wales, Australia: a new high density dataset reveals local stress rotations, *Basin Research*, 29, 622–
899 640, <https://doi.org/10.1111/bre.12175>, 2017c.

900 Rajabi, M., Ziegler, M., Heidbach, O., Mukherjee, S., and Esterle, J.: Contribution of mine borehole data toward
901 high-resolution stress mapping: An example from northern Bowen Basin, Australia, *International Journal of Rock*
902 *Mechanics and Mining Sciences*, 173, 105630, <https://doi.org/10.1016/j.ijrmms.2023.105630>, 2024.

903 Reisdorf, A. G., Wetzel, A., Schlatter, R., and Jordan, P.: The Staffelegg Formation: a new stratigraphic scheme
904 for the Early Jurassic of northern Switzerland, *Swiss Journal of Geosciences*, 104, 97–146,
905 <https://doi.org/10.1007/s00015-011-0057-1>, 2011.

906 Reiter, K. and Heidbach, O.: 3-D geomechanical–numerical model of the contemporary crustal stress state in the
907 Alberta Basin (Canada), *Solid Earth*, 5, 1123–1149, <https://doi.org/10.5194/se-5-1123-2014>, 2014.

908 Reiter, K., Heidbach, O., and Ziegler, M. O.: Impact of faults on the remote stress state, *Solid Earth*, 15, 305–327,
909 <https://doi.org/10.5194/se-15-305-2024>, 2024.

910 Richardson, R. M., Solomon, S. C., and Sleep, N. H.: Tectonic stress in the plates, *Reviews of Geophysics*, 17,
911 981–1019, <https://doi.org/10.1029/RG017i005p00981>, 1979.

912 Roberts, D. and Myrvang, A.: Contemporary stress orientation features and horizontal stress in bedrock,
913 Trøndelag, central Norway, *NGU Bull.*, 442, 53–63, 2004.

914 Roche, V., Camanni, G., Childs, C., Manzocchi, T., Walsh, J., Conneally, J., Saqab, M. M., and Delogkos, E.:
915 Variability in the three-dimensional geometry of segmented normal fault surfaces, *Earth-Science Reviews*, 216,
916 103523, <https://doi.org/10.1016/j.earscirev.2021.103523>, 2021.

917 Saucier, F., Humphreys, E., and Weldon II, R.: Stress near geometrically complex strike-slip faults: Application
918 to the San Andreas Fault at Cajon Pass, southern California, *Journal of Geophysical Research: Solid Earth*, 97,
919 5081–5094, <https://doi.org/10.1029/91JB02644>, 1992.

920 Schmid, S. M., Pfiffner, O. A., Froitzheim, N., Schönborn, G., and Kissling, E.: Geophysical-geological transect
921 and tectonic evolution of the Swiss-Italian Alps, *Tectonics*, 15, 1036–1064, <https://doi.org/10.1029/96TC00433>,
922 1996.

923 Schmid, S. M., Pfiffner, O. A., Schönborn, G., Froitzheim, N., and Kissling, E.: Integrated cross section and
924 tectonic evolution of the Alps along the Eastern Traverse., in: *Deep Structure of the Alps, Results from NFP 20*,
925 edited by: Pfiffner, O. A., Lehner, P., Heitzmann, P., Müller, S., and Steck, A., Birkhäuser Verlag, Birkhäuser,
926 Basel, 289–304, 1997.

927 Schoenball, M., Dorbath, L., Gaucher, E., Wellmann, J. F., and Kohl, T.: Change of stress regime during
928 geothermal reservoir stimulation, *Geophysical Research Letters*, 41, 1163–1170,
929 <https://doi.org/10.1002/2013GL058514>, 2014.

930 Seithel, R., Gaucher, E., Mueller, B., Steiner, U., and Kohl, T.: Probability of fault reactivation in the Bavarian
931 Molasse Basin, *Geothermics*, 82, 81–90, <https://doi.org/10.1016/j.geothermics.2019.06.004>, 2019.

932 Sibson, R., Ghisetti, F., and Ristau, J.: Stress Control of an Evolving Strike-Slip Fault System during the 2010–
933 2011 Canterbury, New Zealand, Earthquake Sequence, *Seismological Research Letters*, 82, 824–832,
934 <https://doi.org/10.1785/gssrl.82.6.824>, 2011.

935 Sibson, R. H.: Implications of fault-valve behaviour for rupture nucleation and recurrence, *Tectonophysics*, 211,
936 283–293, [https://doi.org/10.1016/0040-1951\(92\)90065-E](https://doi.org/10.1016/0040-1951(92)90065-E), 1992.

937 Sinclair, H. D. and Allen, P. A.: Vertical versus horizontal motions in the Alpine orogenic wedge: stratigraphic
938 response in the foreland basin, *Basin Research*, 4, 215–232, <https://doi.org/10.1111/j.1365-2117.1992.tb00046.x>,
939 1992.

940 Smart, K. J., Ferrill, D. A., Morris, A. P., and McGinnis, R. N.: Geomechanical modeling of stress and strain
941 evolution during contractional fault-related folding, *Tectonophysics*, 576–577, 171–196,
942 <https://doi.org/10.1016/j.tecto.2012.05.024>, 2012.

943 Sommaruga, A., Eichenberger, U., and Marillier, F.: Seismic Atlas of the Swiss Molasse Basin, *Matériaux pour la
944 Géologie de la Suisse – Géophysique*, 2012.

945 Stromeyer, D., Heidbach, O., and Ziegler, M.: Tecplot 360 Add-on GeoStress v. 2.0. V. 2.0, GFZ Data Services
946 [code], <https://doi.org/10.5880/wsm.2020.001>, 2020.

947 Su, S. and Stephansson, O.: Effect of a fault on in situ stresses studied by the distinct element method, International
948 Journal of Rock Mechanics and Mining Sciences, 36, 1051–1056, [https://doi.org/10.1016/S1365-1609\(99\)00119-7](https://doi.org/10.1016/S1365-1609(99)00119-7), 1999.

950 Tanner, D. C. and Brandes, C.: Chapter 1 - Introduction, in: Understanding Faults, edited by: Tanner, D., and
951 Brandes, C., Elsevier, 1–10, <https://doi.org/10.1016/B978-0-12-815985-9.00001-1>, 2020.

952 Tavener, E., Flottmann, T., and Brooke-Barnett, S.: In situ stress distribution and mechanical stratigraphy in the
953 Bowen and Surat basins, Queensland, Australia, Geological Society, London, Special Publications, 458, 31–47,
954 doi:10.1144/SP458.4, 2017.

955 Tingay, M. R. P., Hillis, R. R., Morley, C. K., King, R. C., Swarbrick, R. E., and Damit, A. R.: Present-day stress
956 and neotectonics of Brunei: Implications for petroleum exploration and production, AAPG Bulletin, 93, 75–100,
957 <https://doi.org/10.1306/08080808031>, 2009.

958 Treffeisen, T. and Henk, A.: Representation of faults in reservoir-scale geomechanical finite element models – A
959 comparison of different modelling approaches, Journal of Structural Geology, 131, 103931,
960 <https://doi.org/10.1016/j.jsg.2019.103931>, 2020.

961 Vadacca, L., Rossi, D., Scotti, A., and Buttinelli, M.: Slip Tendency Analysis, Fault Reactivation Potential and
962 Induced Seismicity in the Val d'Agri Oilfield (Italy), Journal of Geophysical Research: Solid Earth, 126,
963 2019JB019185, <https://doi.org/10.1029/2019JB019185>, 2021.

964 Viganò, A., Ranalli, G., Andreis, D., and Martin, S.: Inversion for the static friction coefficient of seismogenic
965 faults: Application to induced seismicity of the Basel Enhanced Geothermal System, Switzerland, Journal of
966 Geodynamics, 145, 101843, <https://doi.org/10.1016/j.jog.2021.101843>, 2021.

967 Yale, D. P.: Fault and stress magnitude controls on variations in the orientation of in situ stress, in: Fracture and
968 In-Situ Stress Characterization of Hydrocarbon Reservoirs, edited by: Ameen, M., Geological Society of London,
969 0, <https://doi.org/10.1144/GSL.SP.2003.209.01.06>, 2003.

970 Yale, D. P., Rodriguez, J. M., Mercer, T. B., and Blaisdell, D. W.: In-situ Stress Orientation and the Effects of
971 Local Structure – Scott Field, North Sea, Rock Mechanics in Petroleum Engineering, Delft, Netherlands, 29–31
972 Aug, <https://doi.org/10.2118/28146-MS>, 1994.

973 Yale, D. P. and Ryan, T. C.: In-Situ Stress and Hydraulic Fracture Orientation in the Mid-Continent Area, US, 1st
974 North American Rock Mechanics Symposium, Austin, Texas, 1–3 June, 1994.

975 Yale, D. P., Strubhar, M. K., and El Rabaa, A. W.: Determination of Hydraulic Fracture Direction, San Juan Basin,
976 New Mexico, SPE Production Operations Symposium, Oklahoma City, Oklahoma 21–23 March,
977 <https://doi.org/10.2118/25466-MS>, 1993.

978 Yan, H., Bakk, A., Holt, R. M., and Lozovskyi, S.: Numerical analysis of stress path evolution in the overburden of
979 depleting reservoirs: a parametric study, Geomechanics and Geophysics for Geo-Energy and Geo-Resources, 11,
980 91, 10.1007/s40948-025-00989-5, 2025.

981 Zakhrova, N. V. and Goldberg, D. S.: In situ stress analysis in the northern Newark Basin: Implications for
982 induced seismicity from CO₂ injection, Journal of Geophysical Research: Solid Earth, 119, 2362–2374,
983 <https://doi.org/10.1002/2013JB010492>, 2014.

984 Zang, A. and Stephansson, O.: Stress field of the earth's crust, 2010, Springer Dordrecht, New York, NY, 324 pp.,
985 <https://doi.org/10.1007/978-1-4020-8444-7>, 2010.

986 Ziegler, M. O. and Heidbach, O.: The 3D stress state from geomechanical-numerical modelling and its
987 uncertainties: a case study in the Bavarian Molasse Basin, Geothermal Energy, 8, 11,
988 <https://doi.org/10.1186/s40517-020-00162-z>, 2020.

989 Ziegler, M. O. and Heidbach, O.: Python Script PyFAST Calibration v.1.0 V. 1.0, GFZ Data Services [code],
990 <https://doi.org/10.5880/wsm.2021.003>, 2021.

991 Ziegler, M. O., Heidbach, O., Reinecker, J., Przybycin, A. M., and Scheck-Wenderoth, M.: A multi-stage 3-D
992 stress field modelling approach exemplified in the Bavarian Molasse Basin, *Solid Earth*, 7, 1365–1382,
993 <https://doi.org/10.5194/se-7-1365-2016>, 2016.

994 Ziegler, M. O., Seithel, R., Niederhuber, T., Heidbach, O., Kohl, T., Müller, B., Rajabi, M., Reiter, K., and Röckel,
995 L.: Stress state at faults: the influence of rock stiffness contrast, stress orientation, and ratio, *Solid Earth*, 15, 1047–
996 1063, <https://doi.org/10.5194/se-15-1047-2024>, 2024.

997 Ziegler, M. O., Ziebarth, M., and Reiter, K.: Python Script Apple PY v1.3. V. 1.3,
998 <https://doi.org/10.5880/wsm.2020.002>, 2020.

999 Zoback, M. and Healy, J.: Friction, faulting and in situ stress, *Annales geophysicae* (1983), 2, 689–698, 1984.

1000 Zoback, M., Hickman, S., Ellsworth, W., and the, S. S. T.: Scientific Drilling Into the San Andreas Fault Zone -
1001 An Overview of SAFOD's First Five Years, *Sci. Dril.*, 11, 14–28, <https://doi.org/10.2204/iodp.sd.11.02.2011>,
1002 2011.

1003 Zoback, M. D.: *Reservoir Geomechanics*, Cambridge University Press, Cambridge,
1004 <https://doi.org/10.1017/CBO9780511586477>, 2009.

1005 Zoback, M. D., Zoback, M. L., Mount, V. S., Suppe, J., Eaton, J. P., Healy, J. H., Oppenheimer, D., Reasenberg,
1006 P., Jones, L., Raleigh, C. B., Wong, I. G., Scotti, O., and Wentworth, C.: New Evidence on the State of Stress of
1007 the San Andreas Fault System, *Science*, 238, 1105–1111, <https://doi.org/10.1126/science.238.4830.1105>, 1987.

1008 Zoback, M. L.: First- and second-order patterns of stress in the lithosphere: The World Stress Map Project, *Journal*
1009 *of Geophysical Research: Solid Earth*, 97, 11703–11728, <https://doi.org/10.1029/92JB00132>, 1992.

1010 Zoback, M. L., Zoback, M. D., Adams, J., Assumpção, M., Bell, S., Bergman, E. A., Blümling, P., Brereton, N.
1011 R., Denham, D., Ding, J., Fuchs, K., Gay, N., Gregersen, S., Gupta, H. K., Gvishiani, A., Jacob, K., Klein, R.,
1012 Knoll, P., Magee, M., Mercier, J. L., Müller, B. C., Paquin, C., Rajendran, K., Stephansson, O., Suarez, G., Suter,
1013 M., Udiás, A., Xu, Z. H., and Zhizhin, M.: Global patterns of tectonic stress, *Nature*, 341, 291–298,
1014 <https://doi.org/10.1038/341291a0>, 1989.

1015